A&A 414, 677–697 (2004)
DOI: 10.1051/0004-6361:20031579

Astronomy & Astrophysics

On the analysis of band 3 of the ISO–SWS calibration sources⋆

R. Van Malderen[1], L. Decin[1,⋆⋆], D. Kester[2], B. Vandenbussche[1], C. Waelkens[1], J. Cami[3], and R. F. Shipman[2]

[1] Instituut voor Sterrenkunde, KU Leuven, Celestijnenlaan 200B, 3001 Leuven, Belgium
[2] Space Research Organization Netherlands, PO Box 800, 9700 AV Groningen, The Netherlands
[3] NASA Ames Research Center, Mail Stop 245-6, Moffett Field, CA 94035-1000, USA

Received 2 January 2003 / Accepted 2 October 2003

Abstract. We analyse ISO–SWS 01 ($R \sim 1500$) 12–27.5 μm (band 3) spectra of the 10 standard calibration stars with the highest flux using synthetic spectra generated from (MARCS) atmosphere models. The comparison between the observed and synthetic spectra reveals the quality of (1) the atmospheric model construction and subsequent synthetic spectra computation and of (2) the (OLP 10.1) calibration and data reduction of the spectrometer at these wavelengths.
The models represent the general features of the observations, but the synthetic spectrum computation is hampered by the lack of comprehensive molecular and atomic line lists. We also suspect some problems with the temperature distribution in the outer layers of the model and inaccuracies in the extrapolation of the collision-induced absorption coefficients of H_2 pairs. We detect baseline ripples and fringes in the observed spectra, that survive the calibration and detailed reduction process. Photometric calibration uncertainties are estimated by means of the scaling factors between the synthetic and observed spectra.

Key words. stars: atmospheres – stars: fundamental parameters – instrumentation: spectrographs – molecular data

1. Introduction

The theoretical modelling of the spectra of bright, mostly cool giants, obtained with the SWS (Short Wavelength Spectrometer, covering the spectral range 2.38–45.2 μm, de Graauw et al. 1996), is a diagnostic tool for the accuracy of the calibration of the spectrometer, the state-of-the-art modelling of stellar atmospheres, and the synthesisation of model spectra. The availability of reliable model spectra can lead to major improvements in the calibration of SWS. Vice versa, observed, well calibrated, spectra can indicate discrepancies in the synthetic spectrum computation. To facilitate the diagnosis of the detected discrepancies between synthetic and observed spectra, a reasonable estimate of the reliability of both is required. In order to test the model structure and the fundamental parameters of the model atmospheres, one can also rely on, e.g., IRAS data in addition to the SWS observations.

The results discussed in this paper are the long wavelength (12–27.5 μm) continuation of the research carried out by Decin (2000), Decin et al. (2000, 2003c,b,a) for band 1 (2.38–4.08 μm) and band 2 (4.08–12.0 μm). The comparison of the ISO–SWS spectra with the synthetic spectra in band 1 led to the accurate determination of the stellar parameters of cool giants. The presence of many molecules in the 2.38–4.08 μm range whose band strengths are sensitive to different fundamental stellar parameters, favours this determination. The remaining discrepancies are at the 1–2% level. This proves not only that the calibration of the high-flux sources reached a very satisfying level of accuracy in this band, but also that the description of the cool-star atmospheres and molecular line lists are very accurate. In band 2 severe memory effects and inaccuracies of the Relative Spectral Response Function (RSRF hereafter) limit the relative accuracy to about 6% (Decin et al. 2003c,b,a).

The same level of accuracy cannot not be reached in the longer wavelength range of SWS. The main causes are the lower signal-to-noise ratio of the cool-giant spectra, the growing incompleteness of molecular and atomic line lists with longer wavelengths, and a more problematic calibration of the SWS detectors. Nevertheless, a study limited to more global discrepancies between models and observations in band 3 remains useful (1) to improve our knowledge on the occurrence of molecular lines in the mid-IR, (2) to construct theoretical models and hence synthetic spectra enabling to use these spectra as calibration references next to stellar templates for future IR missions and instruments, and finally (3) to point out specific calibration problems of SWS band 3.

This article is organised as follows. We first specify the selection criteria for the sample in Sect. 2. Then, in Sect. 3, we describe our method of analysis by giving the details of our data reduction and of the different steps in the modelling procedure. In Sect. 4, the results are presented in three parts: firstly, the relative contribution of the different species in the range 12–27.5 μm is shown for 3 example stars, and we emphasise the effective temperatures for which the OH/H_2O and

Send offprint requests to: R. Van Malderen,
e-mail: Roeland.VanMalderen@ster.kuleuven.ac.be

⋆ Based on observations with ISO, an ESA project with instruments funded by ESA Member States (especially the PI countries France, Germany, The Netherlands and the UK) and with the participation of ISAS and NASA.

⋆⋆ Postdoctoral Fellow of the Fund for Scientific Research, Flanders.

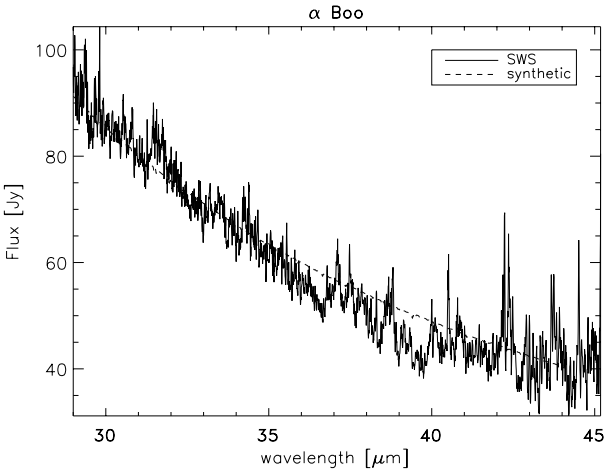

Fig. 1. Example of the ISO–SWS band 4 spectrum of α Boo, the brightest star of our sample.

atomic/molecular contributions change in importance in the considered wavelength range; secondly, the effects of changing stellar parameters within their uncertainties are investigated; thirdly, these results are used to find and discuss the causes of the discrepancies between the observed and computed spectra. Finally, in Sect. 5, we briefly list our conclusions and discuss their usefulness for future IR space missions.

2. Observations

The calibration sources discussed here mainly belong to two different proposals, i.e. STARMOD and ZZSTARM, which were specifically submitted for our purpose. The database was extended by including calibration data provided by the SWS Instrument Dedicated Team (SIDT). This compilation resulted in 16 stars, ranging from spectral types A0 till M2.5 (see Decin et al. 2003c, for more details). For several stars, the flux density in the mid-IR turned out to be too low for our purposes. We therefore restricted our study to 10 stars from the original sample. The result is a spectral type range from A1 till M2.5, the hottest star being Sirius and the coolest β Peg (Table 2).

3. Method of analysis

3.1. Data reduction

The data were obtained using the SWS Astronomical Observation Template (AOT) 01 observing mode which provides full-grating spectra from 2.38 to 45.2 μm. The wavelength range from 12 till 27.5 μm corresponds to the SWS bands – 3A (12−16.5 μm), 3C (16.5−19.5 μm) and 3D (19.5−27.5 μm). Even for bright stars, the spectra in the longer-wavelength bands 3E and 4 have too low a signal-to-noise ratio (<10) for the purpose of this paper, as can be seen in Fig. 1. The measurements we rely on most strongly in this paper, were carried out at the lowest possible scanner speed (= highest possible resolution, speed number 4) of the AOT 01 observing mode. Higher scanner speed observations, denoted by decreasing speed numbers 3 to 1, were only used marginally. The spectral resolution $\lambda/\Delta\lambda$ of our speed 4 spectra then varies from about 1150 (3A), over about 1800 (3C) to about 1000 for band 3D (Lorente 1998). The spectra were reduced with the SWS Interactive Analysis package developed by the SWS Instrument Dedicated Team (SIDT) using all standard routines of the final Off-Line Processing (OLP) 10.1 to obtain the Auto-Analysis Result (AAR), with the exception that we used the command `resp_inter` instead of `respcal` (see Sect. 3.1.2) to perform a first rough fringes removal simultaneously with the responsivity calibration. The AAR is the end product of the SWS pipeline and contains for each detector a fully calibrated spectrum for each of the two scans (the up- and downscan), i.e. flux (in Jy) vs. wavelength (in μm). Further steps are required to combine these spectra of the individual detectors and both scans for each band into one spectrum of the highest possible quality.

On the AAR structure we discarded the data of the detectors within one spectral scan when they differed too much from the combined data of all detectors. Glitches were simultaneously removed. A detailed analysis between the differences in up- and downscan enabled us to expel scan jumps, which are sudden flux changes in all detectors of a detector block. All data (parts) of remaining detectors and scans were then flatfielded to one another. Other bad data points were removed by sigma clipping, with the varying kappa-sigma value (depending on the number of points in the array) obtained by the application of Chauvenet's criterion: "A measurement may be excluded when the chance that such a measurement falls in a series of N measurements is smaller then $1/2N$". This reduces the number of data points by typically 2−4% in band 3. The residual fringes were handled with the procedure `fringes` (see Sect. 3.1.2). The final spectra were obtained by rebinning to the estimated resolution of each band at an oversampling rate of 4, and by joining the different subbands (i.e. 3A, 3C, and 3D).

It should be noted that in the whole process of data manipulation, we took special care not to discard real data points. To that aim, special attention was paid to the comparison of the response of the individual detectors and scans. The reduction results in spectra of signal-to-noise ratios of about 40–50 for bands 3A, 3C, and 3D in the case of our observations, and somewhat lower at the band edges, where the RSRF correction is more problematic. Below, we describe in some more detail the most decisive of these additional reduction steps we performed on the AAR, and comment on our choice of including them in the reduction process.

3.1.1. Removal of bad detector data points, glitches, and scan jumps

The use of sigma clipping does not suffice to cancel out all features originating from glitches or bad detector data points. In particular, the rather bad agreement between the up- and downscan for the majority of our sample stars led to the integration of a comparison of the data of all detectors and scans in our reduction process, using an interactive tool developed by Cami (2002). The tool will probably become part of the SWS data reduction package.

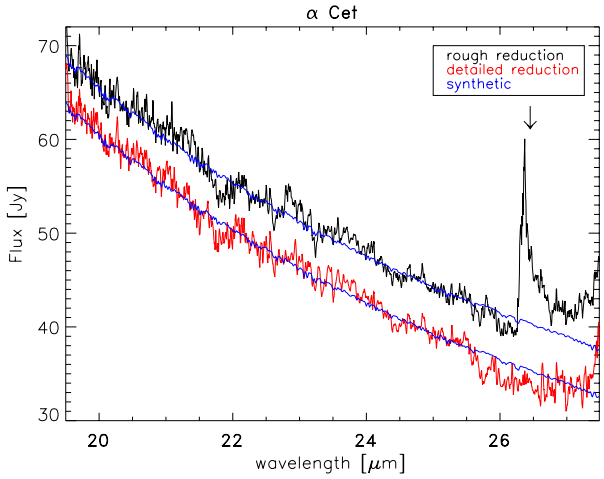

Fig. 2. Comparison for α Cet between the rather standard OLP10.1 reduction method (upper black) and our detailed reduction which includes a thorough check of all detectors and both scans (lower black). It should be noted that the more detailed reduced spectrum has lower uncertainties on the individual points and that it agrees "better" with the synthetic spectrum (grey). A glitch, marked by the arrow, is efficiently removed through our reduction, while it remains present in the data after the automatic mode reduction. The noticed discrepancies between the synthetic and observed spectrum will be extensively discussed later in this paper.

With this tool, the spectrum recorded by one detector has been be compared with the combined spectra of all detectors, allowing straightforward detection of glitches and bad detectors. In a different mode, raw or rebinned data from the up and down scans can be compared in order to detect scan jumps. When we finally compared the roughly and more detailed reduced spectra with our synthetic spectra, we found that using the tool improves the spectrum by about 2% in band 3A, by 2.5% in band 3C, by 4% in band 3D, and by up to 10% at the band edges. An example is given in Fig. 2.

3.1.2. Fringes removal

Fringes are a modulation with wavelength of the flux falling on the detectors and originate on parallel-plane surfaces in the light path which act as Fabry-Pérot (FP) etalons; they present a considerable nuisance in the reduction of ISO spectra (Leech et al. 2003). Although the SWS pipeline is designed to remove them, residual fringe patterns of up to 10% may be left in some bands. The pipeline attempt (the routine `respcal`) to remove the fringes is made when dividing the SWS data with the Relative Spectral Response Function (RSRF). Since the RSRF characterises the wavelength-dependent response of the SWS, it also contains fringes, and it was expected that fringes would be divided out when executing the responsivity calibration. However, there are two main reasons why in practice fringe residuals are left after applying this reduction step. First, the resolution of our slow AOT 01 speed 4 data of point sources is often higher than that of the RSRF, which is partly based on laboratory measurements using a black body source which filled the slit completely. The combination of the smaller size and the lower scanner speeds for our observations results in stronger fringe amplitudes in our data, which are thus not properly cancelled out by division with the more smoothed RSRF. Secondly, the fringes in the data may be shifted in wavelength with respect to those in the RSRF, depending on where the source is on the slit, especially in the dispersion direction. As different components of the fringe pattern shift by different numbers, a complex fringe pattern results.

The procedure `resp_inter` in the SWS Interactive Analysis package tries to correct these shortcomings of the RSRF by allowing it to be shifted in wavelength and to enhance/smooth the amplitude of its fringes, both with respect to the specific input spectrum. Another fringe removal procedure, `fringes`, executes (convolutions of) cosine fitting through the wavenumber space of the data. It detects fringes in wavenumber space, as they should have a constant frequency (in cycles per wavenumber) there. A range in frequencies, known to be present in the RSRF, is searched for and the minimum in χ^2 then determines the fringe which is most likely to be present in the data. The Bayesian evidence for this fringe is then calculated. If this evidence is larger than the evidence carried by the previous set of fringes, the fringe is kept and a new fringe component is identified; if not, the total fringe set, with proper amplitudes, is subtracted from the data (Cami 2002). Different modes of `fringes` can be used, and the default mode executes a defringing with all data per band combined. Alternatively, each individual detector or the up- and downscans can be defringed separately. Even for our speed number 4 data, there are not enough data points in the observations to defringe each individual detector separately. The same problem arises in the case of removing the fringes of the up- and downscan separately for speed 1 and 2 data. Additionally, the choice between either combining the up- and downscans or treating both scans separately in the defringing process can be made on a statistical basis, by means of the Bayesian evidence. We found that, in general, for our speed 4 observations the default mode is the best option.

Although, at first sight, the routine `resp_inter` seems to be the correct way of dealing with the fringing problem, `fringes` turns out to be the most powerful one for the observations presented in this paper, as can be seen in Fig. 3. Cami (2002) reached the same conclusion for his SWS AOT 01 all speeds data. Nevertheless, as `resp_inter` and `fringes` are complementary routines, in the sense that the "cleaner" spectrum returned after using `resp_inter` instead of `respcal` allows a better defringing with `fringes`, we used both routines in our reduction strategy. Especially in band 3A, the combination of both routines decreases in some cases the number of fringe residuals with regard to using only `fringes`.

3.1.3. Joining the subbands

As the flatfield calibration of the longer wavelength part of the SWS has not been fully optimised yet, we had to shift the different individual subbands (i.e. 3A, 3C and 3D) in flux w.r.t. each other in order to obtain a reasonably smooth spectrum. This shift can be performed by using either a multiplicative scaling

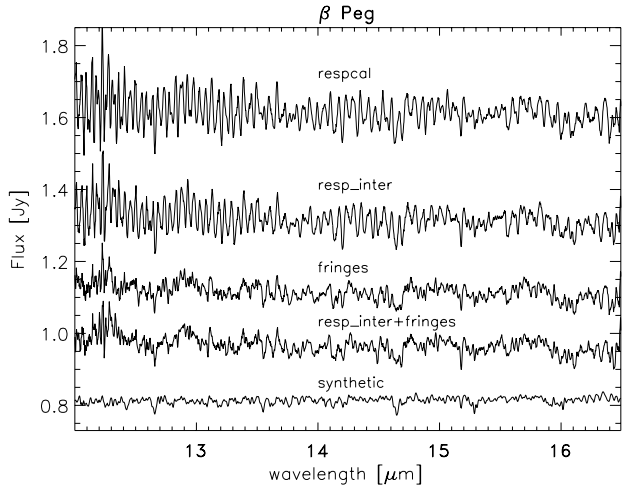

Fig. 3. Overview of the band 3A spectra of β Peg, reduced by using `resp_inter` and/or `fringes`, i.e. two different fringe removal tools which are at the disposal of the SWS user, together with the pipeline attempt to remove fringes (`respcal`).

or an additive. As the main causes of the band-to-band discontinuities (see Sect. 4.3.2) change the flux in a band by a gain factor, we applied scaling factors. Several ways exist to join the different band spectra. A first method glues the different subbands to one another by using the small overlap region between adjacent bands. Decin et al. (2003c) argue to take band 1D as reference. Starting from band 1D, the average flux in the overlap regions for neighbouring subbands is determined, and these averages are used to pin down a scaling factor for the adjacent subbands. After scaling, the same method can be applied to the next subband (Cami 2002).

In our analysis, the synthetic spectra were used to combine the different band 3 subband spectra into one continuous spectrum. In order to do so, we calculated for each subband the weighted mean of the division of the reduced SWS spectrum by the synthetic spectrum, the weights being equal to the square of the inverse normalised uncertainties on the individual points, as calculated through the rebinning process. Scaling factors were then defined as the reciprocal of these weighted means. We did not determine the uncertainties on the points in the way they are calculated through the pipeline rebinning (and stocked in the STDEV tag of the AAR structure), but kept the largest error estimate available. If both an up- and a downscan survived our reduction, the difference between the two was taken as the error, unless the STDEV value was larger. The weighted scaling factors are listed in Table 1 and will be discussed later in this paper.

The average SWS user does not dispose of a set of synthetic model spectra of her/his studied objects and so has to rely on the first described method. Due to the low responsivity at the band edges and the memory effects in band 2, this method can lead to substantial errors in band 3. That the method based on synthetic spectra leads to reliable results, will be further elaborated in Sects. 3.2 and 4.3.1. In order to quantify the possible errors due to inadequate band matching, we have compared the results from both procedures for all our observations. It turns out that, on average, the glued spectrum is shifted by respectively 8.5%, 9%, and 10% in bands 3A, 3C, and 3D, w.r.t. the synthetic spectrum. The highest scaling factors (up to 20%) occur for the speed 1 observations, for which the uncertainties in the responsivity at the band edges are largest, and the speed 4 observations (up to 15%), because these data have the highest flux levels and are most affected by memory effects in band 2. Clearly, these uncertainties must be kept in mind when deriving photospheric continua from the SWS spectra, for example in order to measure dust features in this wavelength range.

Table 1. Weighted scaling factors for the individual bands for different measurements of our program stars.

star	AOT number	speed	3A	3C	3D
α CMa	68901202	4	0.97	0.95	0.90
α Car	72902207	4	0.99	1.06	1.03
α Cen A	29400809	1	0.77	0.85	0.77
	60702006	4	1.00	1.00	0.91
α Boo	27503811	1	0.95	0.92	0.93
	45200101	4	1.10	1.09	1.11
β UMi	18205639	4	0.90	0.98	0.95
γ Dra	04002405	4	0.91	0.89	0.80
	12601315	1	0.92	1.10	1.14
	37704637	4	0.98	0.96	0.91
	49603004	1	1.00	0.95	0.94
	81100302	2	1.07	0.98	0.98
α Tau	63602102	4	0.88	0.90	0.83
β And	42301404	2	0.98	1.06	1.04
	44004605	3	0.96	1.03	1.08
	79501002	4	1.11	1.05	1.05
α Cet	79702803	4	0.97	0.99	1.01
	80600924	4	0.97	1.01	0.94
β Peg	05602595	1	0.84	0.82	0.75
	20601346	3	0.95	0.95	0.95
	55100705	4	1.15	1.18	1.19

3.2. Modelling

Obtaining a synthetic spectrum is a two-step process, consisting of the construction of a stellar atmosphere model and subsequently the generation of a synthetic spectrum. The model atmosphere is described by variables (T, P_e, P_g, ρ, etc.) as a function of a chosen depth variable; a detailed radiative transfer calculation then yields the synthetic spectrum. The models used here have been generated with the state-of-the-art MARCS code (Gustafsson et al. 1975; Plez et al. 1992, version May 1998), and the synthetic spectra were obtained using the TurboSpectrum program described by Plez et al. (1993), which shares much of its input with the model construction code.

The atmosphere models adopt a plane-parallel geometry in the cases of α CMa, α Car, and α Cen A, and a spherical stratification for the cooler stars of our sample (see Table 2), hydrostatic equilibrium, and LTE. Energy conservation is required for the total flux, both radiative and convective, the latter being treated through a local mixing-length theory (Henyey et al. 1965). Turbulence pressure is neglected. The Opacity

Table 2. Fundamental stellar parameters for our sample stars as determined by Decin (2000). The effective temperature $T_{\rm eff}$ is given in K, the logarithm of the gravity in cgs units, the microturbulent velocity $\xi_{\rm t}$ in km s^{-1}, the angular diameter in mas, the parallax π in mas, the distance D in parsec, the radius R in $R_\odot$, the gravity-induced mass $M_{\rm g}$ in $M_\odot$ and the luminosity L in $L_\odot$. PP denotes a plane-parallel geometry, SPH a spherical geometry.

	α CMa	α Car	α Cen A	α Boo	β UMi
Sp. type	A1 V	F0 II	G2 V	K2 IIIp	K4 III
$T_{\rm eff}$	10150 ± 400	7350 ± 300	5830 ± 30	4300 ± 70	4150 ± 70
log g	4.30 ± 0.20	1.80 ± 0.50	4.35 ± 0.05	1.50 ± 0.15	1.90 ± 0.15
$\xi_{\rm t}$	2.0 ± 0.5	2.0	1.0 ± 0.1	1.7 ± 0.5	2.0 ± 0.5
[Fe/H]	0.50 ± 0.30	−0.25 ± 0.05	0.25 ± 0.02	−0.50 ± 0.20	−0.15 ± 0.20
ε(C)	7.97 ± 0.15	8.41 ± 0.10	8.74 ± 0.05	7.96 ± 0.15	8.40 ± 0.20
ε(N)	8.15 ± 0.15	8.68 ± 0.05	8.26 ± 0.09	7.55 ± 0.15	8.16 ± 0.20
ε(O)	8.55 ± 0.12	8.91 ± 0.10	9.13 ± 0.06	8.67 ± 0.15	8.83 ± 0.15
^{12}C/^{13}C	89	89	89	7 ± 1	9 ± 1
$\theta_{\rm d}$	6.17 ± 0.27	7.22 ± 0.30	8.80 ± 0.34	20.80 ± 0.83	9.86 ± 0.40
π	379.21 ± 1.58	10.43 ± 0.53	737 ± 2.6	88.85 ± 0.74	25.79 ± 0.52
D	2.63 ± 0.01	95.88 ± 4.87	1.36 ± 0.01	11.26 ± 0.09	38.78 ± 0.78
R	1.75 ± 0.08	74.39 ± 4.89	1.27 ± 0.05	25.24 ± 1.03	41.09 ± 1.87
$M_{\rm g}$	2.23 ± 1.05 (PP)	12.8 ± 6.13 (PP)	1.30 ± 0.46 (PP)	0.74 ± 0.26 (SPH)	4.90 ± 1.90 (SPH)
L	29 ± 4	14571 ± 497	1.7 ± 0.2	196 ± 21	452 ± 48

	γ Dra	α Tau	β And	α Cet	β Peg
Sp. type	K5 III	K5 III	M0 III	M2 III	M2.5 III
$T_{\rm eff}$	3930 ± 70	3850 ± 70	3780 ± 70	3745 ± 70	3590 ± 150
log g	1.55 ± 0.25	1.50 ± 0.15	1.40 ± 0.20	1.30 ± 0.15	1.50 ± 0.40
$\xi_{\rm t}$	2.0 ± 0.5	1.7 ± 0.3	2.3 ± 0.5	2.3 ± 0.5	2.3 ± 0.5
[Fe/H]	0.00 ± 0.20	−0.15 ± 0.20	0.00 ± 0.20	0.00 ± 0.20	0.00 ± 0.30
ε(C)	8.22 ± 0.20	8.35 ± 0.20	8.20 ± 0.20	8.40 ± 0.20	8.56 ± 0.30
ε(N)	8.26 ± 0.20	8.35 ± 0.20	8.37 ± 0.20	8.26 ± 0.20	8.24 ± 0.30
ε(O)	8.81 ± 0.15	8.83 ± 0.15	8.84 ± 0.15	8.93 ± 0.15	9.03 ± 0.30
^{12}C/^{13}C	10 ± 1	10 ± 1	9 ± 1	10 ± 1	7 ± 1
$\theta_{\rm d}$	10.07 ± 0.40	20.77 ± 0.83	13.59 ± 0.55	12.52 ± 0.50	16.88 ± 0.70
π	22.10 ± 0.46	50.09 ± 0.95	16.36 ± 0.76	14.82 ± 0.83	16.37 ± 0.72
D	45.25 ± 0.94	19.96 ± 0.38	61.12 ± 2.84	67.48 ± 3.78	61.08 ± 2.69
R	48.97 ± 2.21	44.63 ± 1.97	89.27 ± 5.50	90.86 ± 6.25	110.52 ± 6.69
$M_{\rm g}$	3.11 ± 1.50 (SPH)	2.30 ± 0.82 (SPH)	7.32 ± 3.48 (SPH)	6.02 ± 2.89 (SPH)	14.12 ± 6.73 (SPH)
L	516 ± 59	395 ± 45	1468 ± 211	1465 ± 229	1830 ± 300

Sampling (OS) method (Sneden et al. 1976) is used to calculate atomic and molecular opacities in approximately 95 000 wavelength points over the wavelength range 1300 Å−20 μm. Decreasing the number to 12 500 points causes maximal differences as low as 0.025% between the synthetic spectra. For the opacity sources included in the MARCS code, we refer to Decin (2000) or Ryde & Eriksson (2002).

For the computation of synthetic spectra from the model atmospheres we used extensive line lists found in the literature. The radiative transfer computations were performed for points separated by $\Delta\lambda \sim 0.75$ km s^{-1}, corresponding with a spectral resolution $\lambda/\Delta\lambda \sim 400\,000$, and the final synthetic spectra were rebinned to the much lower SWS resolution. The microturbulent velocity $\chi_{\rm t} \sim 2$ km s^{-1} which was adopted is much less than the total line broadening, which implies that we sample all lines in our database. This is especially important when dealing with molecular bands, since the separation between lines varies greatly with wavelength, depending on whether the lines are close to a band head or not (Ryde & Eriksson 2002). Our confidence in the chosen wavelength spacing is strengthened by the comparison of two final synthetic spectra of β Peg, calculated from two different wavelength grids, with $\Delta\lambda \sim 0.75$ and ∼0.15 km s^{-1} respectively. β Peg was chosen because it exhibits the strongest molecular lines of our sample.

The difference between the two synthetic spectra at SWS resolution is at most 0.5%! A last note concerns the long wavelengths. The construction of atmosphere models is only developed out to 20 μm (the wavelength range for the Opacity Sampling), and the extrapolation of the model beyond this wavelength may cause uncertainties, that obviously increase with wavelength. We will come back to this later.

In the remaining of this section, we focus on the stellar parameters and the line opacity data of the synthetic spectra. Special emphasis is given to a critical analysis through a comparison with external data, i.e. the IRAS data in the case of the stellar parameters, and line opacity data in other than our line lists.

3.2.1. Stellar parameters

A MARCS model requires as input the effective temperature, the gravity, the metallicity, the mass, the microturbulent velocity and the chemical composition of the star one wants to model. We assume solar abundances from Anders & Grevesse (1989), except for C, N, and O and for the solar iron abundance where we prefer the value $\epsilon(\mathrm{Fe})_{\odot} = 7.51$, in better agreement with the meteoritic value; the CNO abundances, as well as the other stellar parameters, are taken from the literature. These estimates are then refined by requiring agreement between the SWS spectrum and a synthetic spectrum in the wavelength range 2.38−4.08 μm (band 1 of ISO–SWS). This band was chosen on the basis of the best flux calibration accuracy of the instrument in band 1, the best signal-to-noise ratio of the spectra, and the absence of harmful instrumental artifacts such as memory effects (Van Malderen et al. 1999; Kester 2003) or fringes (Kester et al. 2003). For more details about the method of stellar parameter determination, we refer to Decin et al. (2000). The stellar parameters used in this study, together with their statistically determined uncertainties, are listed in Table 2.

An independent test on these stellar parameters, especially the effective temperature and/or angular diameter, is provided through the comparison of our MARCS model spectra with IRAS data products, i.e. the IRAS Point Source Catalogue (PSC) Flux Densities at 12 and 25 μm and the IRAS Low Resolution Spectrometer (LRS) spectra. The IRAS-LRS spectra were interactively processed through the Groningen Image Processing SYstem (GIPSY) routine `lrscal` (Assendorp et al. 1995). The comparison between the MARCS synthetic spectra, the (colour corrected) IRAS-PSC fluxes at 12 and 25 μm (together with 1 σ uncertainty values), and the IRAS-LRS spectra is graphically presented in Fig. 4 for the original sample of Decin (2000). In Table 3, the integrated fluxes in the MARCS synthetic spectra, convolved with the IRAS pass-bands, are compared with the IRAS-PSC fluxes at 12 and 25 μm. The comparison between the LRS and the MARCS model spectrum of a given star was quantified as the mean of the quotient of the LRS spectrum with the synthetic spectrum. The latter was in this case convolved with the instrumental (Gaussian) profile (of resolution 40) of the IRAS-LRS instrument. From Fig. 4 and Table 3, we find good agreement between the measured IRAS-PSC flux densities and the model predicted ones, especially at 12 μm. However, in Fig. 4, it can be seen that the error bars of the IRAS-PSC fluxes for several stars are not consistent with the synthetic spectrum. The error bars are the statistical 1 σ uncertainty values; realistic absolute calibration uncertainties are lacking in the PSC. One of us (DK) estimates it at ~20% in the 12 and 25 μm fluxes. The larger uncertainties of the IRAS-LRS spectra are also reflected through our comparison with the MARCS models.

Table 3. Scaling factors between the IRAS-PSC & LRS products and the MARCS model spectra.

Star	IRAS-PSC		IRAS-LRS
	12 μm	25 μm	
α Lyr	1.00	1.20	1.10
α CMa	0.95	1.04	1.05
β Leo	0.95	1.30	0.64
α Car	1.03	1.07	0.94
α Cen A	1.23	1.27	1.54
δ Dra	1.01	1.10	0.74
ξ Dra	1.01	1.10	0.82
α Boo	1.06	0.96	1.35
α Tuc	0.96	1.00	0.85
β UMi	1.02	1.04	0.88
γ Dra	1.01	1.04	0.86
α Tau	1.09	1.00	0.92
HD 149447	0.98	1.01	0.88
β And	1.07	1.05	0.85
α Cet	1.03	1.01	0.88
β Peg	0.99	1.01	0.92

For α Cen A, the deviations between the MARCS models and all IRAS data are rather large, so its composite spectrum developed by Cohen et al. (1996) is considered as well. This composite spectrum is much closer to our synthetic spectrum than the IRAS data, so we suspect a bad calibration of the IRAS data in the case of this star. The high value of the IRAS-PSC at 25 μm in the case of α Lyr is caused by the circumstellar dust disk (Aumann et al. 1984). Large scale factors between the models and the IRAS data occurring for other stars do not display a general trend and are herefore most probably due to specific calibration problems as well, for example resulting from a very low signal-to-noise ratio, as for β Leo. By all means, it is encouraging that the IRAS-LRS spectrum and the synthetic spectrum of an individual star show about the same slope.

3.2.2. Line lists for the generation of synthetic spectra

The line lists (consisting of wavelengths, excitation energies of the lower state of the transition, and line strengths in the form of oscillator strengths) we have used are listed in Table 4. The conversion from the "air" wavelengths in spectroscopic line lists above 200 nm to "vacuum" wavelengths for the SWS observations was made by extending Edlén's formula (Edlén 1966) to the mid-infrared. This extrapolation can lead to uncertainties in the line peak positions. However, no systematic

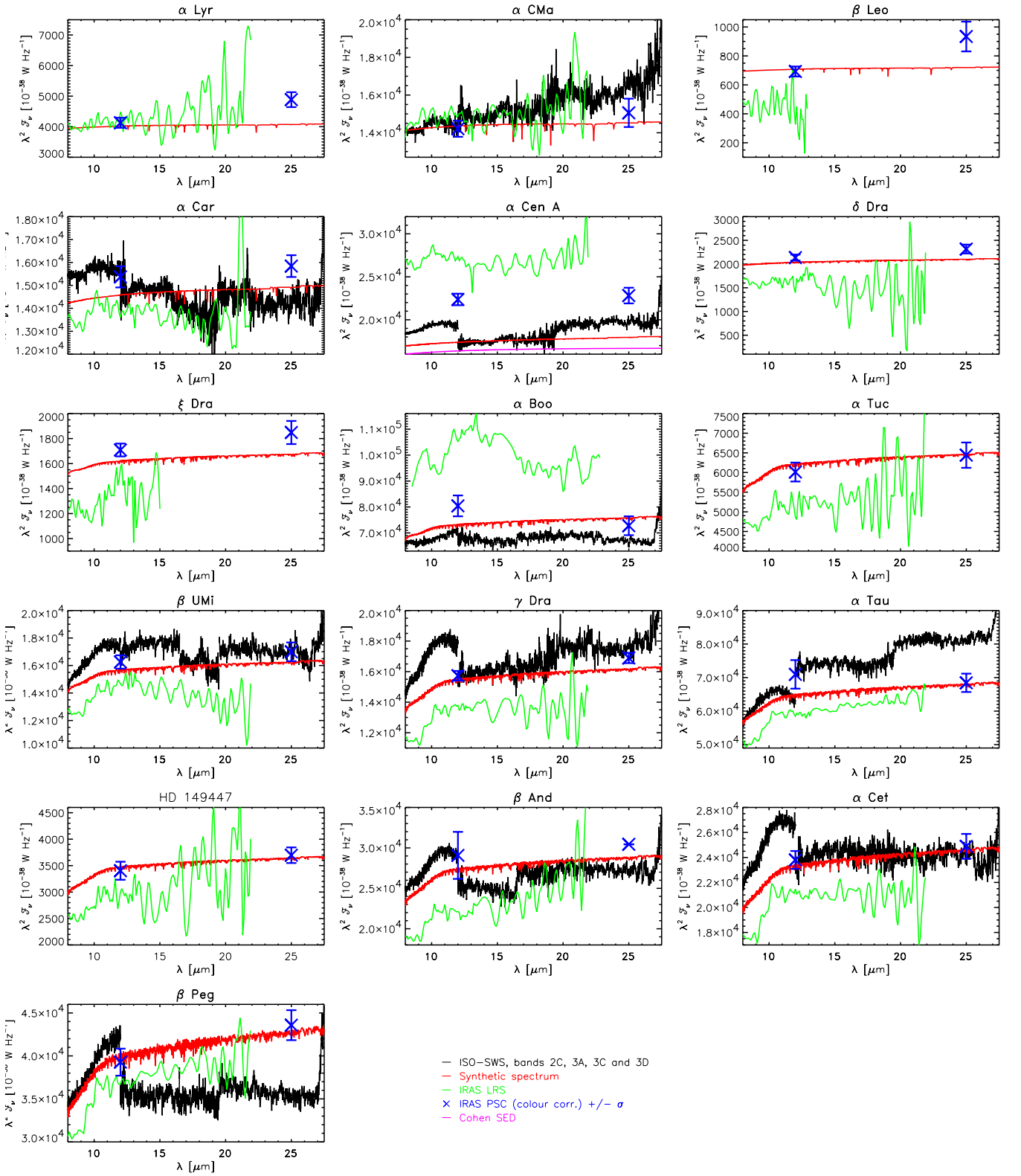

Fig. 4. Comparison between the synthetic spectra at SWS resolution, the (colour corrected) IRAS-PSC fluxes at 12 and 25 μm and the IRAS-LRS spectra. We also plotted the (unshifted) ISO–SWS bands 2C and 3(A till D) spectra for our 10 program stars.

wavelength shift w.r.t. the detectable line peak positions in the observed ($R \sim 1500$) spectra was found.

In the case of OH, two line lists were at our disposal, those by Langhoff et al. (1989) and by Goldman et al. (1998b). We have used the second one, but the differences between using

Table 4. Line lists used for the synthetic spectra.

Species	Ref.
H	Kurucz & Bell (1995)
atoms	Kurucz & Bell (1995)
	van Hoof (1998)
	Hirata & Horaguchi (1995)
CH	Jørgensen et al. (1996)
CN	Plez (private communication),
	dissociation energy = 7.76 eV
CO	Goorvitch (1994)
HCl	Sauval, compilation of
	Le Roy (1999)
	Ogilvie et al. (1980)
	Arunan et al. (1992)
H_2O	AMES (Partridge & Schwenke 1997)
NH	Sauval, compilation of
	Grevesse et al. (1990)
	Geller et al. (1991)
NO	Sauval (Goldman et al. 1998a)
OH	Goldman et al. (1998b)
SiO	Langhoff & Bauschlicher (1993)
TiO	Schwenke (1998)

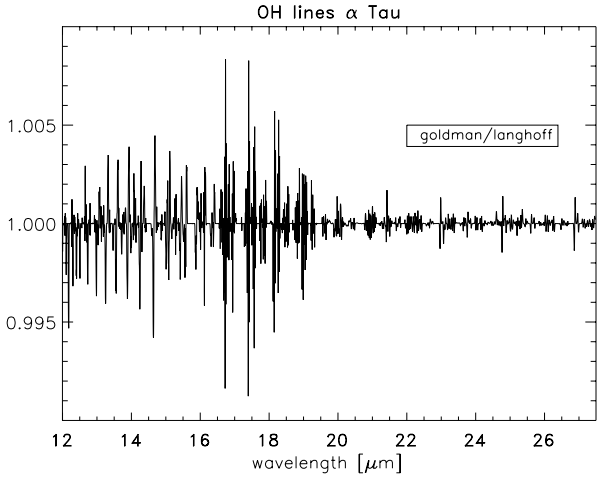

Fig. 5. Relative comparison between the OH synthetic spectra generated by using the line lists at our disposal for α Tau. The used stellar parameters can be found in Table 2.

one or the other are very small (less than 1% in the example of Fig. 5).

In Fig. 6 we made a comparison for **H_2O** in a cool-star model between the synthetic spectra generated by

- the *calculated* MT line list described in Miller et al. (1994), but with the more recent partition functions by Vidler & Tennyson (2000),
- the *"semi-calculated"* (see later) NASA AMES database (Partridge & Schwenke 1997), including all lines stronger than given by the condition $\log gf - \chi\theta \geq -10$, with $\theta = 5040/3500$ and χ the excitation energy in eV,
- the *calculated* SCAN line list (Jørgensen et al. 2001), using the same cut factor as the AMES line list, and
- the *lab data* of the High-Temperature molecular spectroscopic database (HITEMP), i.e. the high-temperature analogue of HITRAN (Rothman et al. 1996, 2003), with the NASA AMES partition functions.

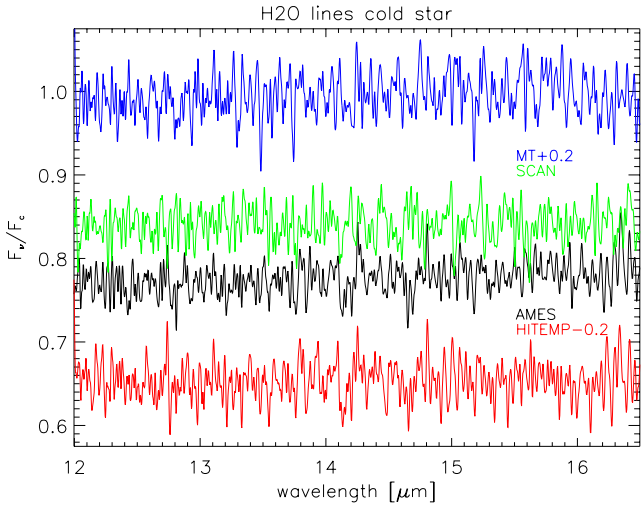

Fig. 6. Comparison between H_2O 12−16.5 μm synthetic spectra, using the different line data at our disposal, for a model star with $T_{\rm eff}$ = 3000 K, log g = 1.00, ξ_t = 2.0 km s^{-1}, [Fe/H] = 0.00, ε(C) = 8.35, ε(N) = 8.35, ε(O) = 8.83, ^{12}C/^{13}C = 10, and M = 2.0 $M_\odot$ in a plane-parallel geometry. The spectra are offset with the values mentioned in the legend. The synthetic spectra have the ISO resolution of band 3A (1150). The references of the line lists can be found in the text.

From Fig. 6, it can be derived that the AMES line list generates a lower H_2O pseudo-continuum than the MT and SCAN line lists do, the mean relative differences w.r.t. the AMES pseudo-continuum being 2.5 and 8.5% respectively. In this context, Schwenke & Partridge (2000) reported on problems with their analytical representation of the ab initio dipole moment data used for the computation of the AMES water list. These problems may have led to an overestimation of the intensities of weak bands with respect to experimental data.

For the comparison of the relative line strengths and the line peak positions, we also included the observational HITEMP database in Fig. 6. This line list aims at conditions of about 1000 K, so that extrapolation to the higher temperatures of stellar atmospheres may be insufficient, due to the lack of high-excited states: a large number of lines may be missing. We made use of the AMES partition functions in the synthetic spectrum generation, as to overcome inaccuracies induced by the extrapolation of the HITEMP ones (calculated up to 3000 K) to higher temperatures for the radiative transfer calculation in the stellar atmosphere. This replacement does not affect the line strengths and positions significantly. From Fig. 6, it can be deduced that there are large variations between the relative line strengths and line peak positions of H_2O lines generated by the MT, SCAN, and AMES databases. The good agreement

between the AMES and HITEMP database is artificial: in the AMES database the potential was first computed purely ab initio and then adjusted until an optimal fit to the line frequencies in the HITRAN line list was obtained.

Taking into account that the MT list is a relatively small list, which used, by today's standards, a rather inaccurate potential (Jones et al. 2002), the remaining question is whether to use the AMES or the SCAN water line list. Both lists are based on the same ab initio theory, but the main difference between both calculations is that the AMES list includes more observational data from the HITRAN database. Opinions diverge in the literature about which list to use. Jørgensen et al. (2001) found a better agreement between the 2.3−4.5 μm ISO–SWS spectrum of the M-type giant star SV Peg and the synthetic spectrum generated with the SCAN line list than with the AMES database. Jones et al. (2002), on the other hand, found a good match of the SWS observations in the 2.5−3.0 μm region for a range of M dwarfs with synthetic spectra based on the AMES line list, but not so with the SCAN line list. The relatively hot temperature scale for M dwarfs they derived from the fits between observations and synthetic spectra, is attributed to the non-physical line splittings of the AMES line list. These splittings lead to synthetic spectra predicting water bands that are too strong for a given temperature. This could be another part of the explanation for the observed lower pseudo-continuum for the AMES line list in our data. Ryde & Eriksson (2002) also used the AMES water vapour line list to synthesise a higher resolution ISO–SWS AOT 06 spectrum of an M giant, and found a good agreement. The disagreement in the literature about which water line list to use, inspired the University College London group to start new calculations on H_2O. Results are not to be expected before at least mid 2004 (Tennyson 2002, private communication). Our choice of the AMES line list is based on its satisfactory predictions for the shorter wavelength part of our SWS spectra (Decin et al. 2003a) and because this list includes observational data.

4. Results

4.1. Relative contribution of the different species

In Figs. 7–9 we show the normalised synthetic spectra for each molecule separately, and also for the atoms, for α Boo, α Tau, and β Peg. Of course, some caution is required here, since neglecting the rest of the molecular (and atomic) opacities might change the geometrical depth where the investigated lines are formed (Aringer et al. 2002). But the figures do illustrate what the main absorbers are in the wavelength range under study here, from OH in α Boo to H_2O in β Peg. In the case of α Tau, H_2O completely determines the pseudo-continuum of its spectrum, but the strongest individual lines are mainly OH lines. Indeed, calculations show that at temperatures lower than 3900 K, water becomes the most important oxygen-containing molecule as well as the dominant opacity source. At solar temperatures water is dissociated, and OH is the main opacity source (Wallace et al. 1995, and references therein).

Other molecules showing absorption bands in our wavelength range are NH, HF, HCl, and SiO, the latter only at the shorter wavelength side in β Peg, i.e. the continuation of the SiO fundamental at 8 μm. The strength of the spectral features of these molecules increases with decreasing temperature (α Boo $\rightarrow$ β Peg): we assumed the same $\log g$-value for these three example stars; the other stellar parameters hardly affect the spectral footprint of a star (see Decin 2000; Decin et al. 2000). Other molecules present in our line lists database, such as CN, CO, CH, NO, and TiO, do not absorb at all in the wavelength range 12−27.5 μm.

A comparison of the synthetic spectra of all the sample stars (see Figs. 10 and 11) reveals that the hottest stars (α CMa and α Car) only have atomic contributions, and that the spectra of cooler stars are dominated by molecular transitions. The transition between the two groups is made by α Cen A, its synthetic spectrum showing almost no lines at ISO–SWS resolution. The coolest star in our sample (β Peg) still has atomic lines in its synthetic spectrum, with strengths comparable to those in the synthetic spectra of α Boo and α Tau. However, the relative weakness of atomic lines compared to molecular lines, the blending of atomic lines with molecular lines and the low resolution and signal-to-noise ratio of the ISO spectra prohibit the identification of atomic lines in the IR spectrum of K or M giants.

4.2. Influence of the uncertainties of stellar parameters on synthetic spectra

The uncertainties on the different stellar parameters listed in Table 2, are statistically derived values, which may underestimate the real uncertainties (see Decin et al. 2003b,a, for more realistic statistical estimates). In order to find out how the global slope of the synthetic spectrum changes when a stellar parameter is altered within realistic uncertainties, we follow Decin et al. (2000), where a similar analysis is performed in the 2.38−12 μm range, with α Tau as the test case. The temperature is varied over 100 K, the logarithmic gravity over 0.2. The change of the synthetic spectrum due to variations of the other parameters is less pronounced.

A temperature decrease by 100 K causes the largest change in the synthetic spectrum ($\sim$1% at 12 μm, less at longer wavelengths). From Figs. 7–9, it can be derived that mainly the increasing H_2O opacity accounts for this change in the synthetic spectrum. An increase of the logarithmic gravity (with 0.2) induces a change which is qualitatively similar to that of the temperature decrease, but the effect is smaller. For hotter stars, showing almost no water absorption in their mid-IR synthetic spectrum, the *global* slope of the spectrum hardly changes within the error bars of the stellar parameters.

4.3. Discussion of the discrepancies between the SWS and modelled spectra

Due to the low signal-to-noise ratio in the wavelength range considered, small-scale discrepancies between our observational spectra and the computed spectra cannot be detected. We therefore must limit the discussion to the detection of global deviant trends.

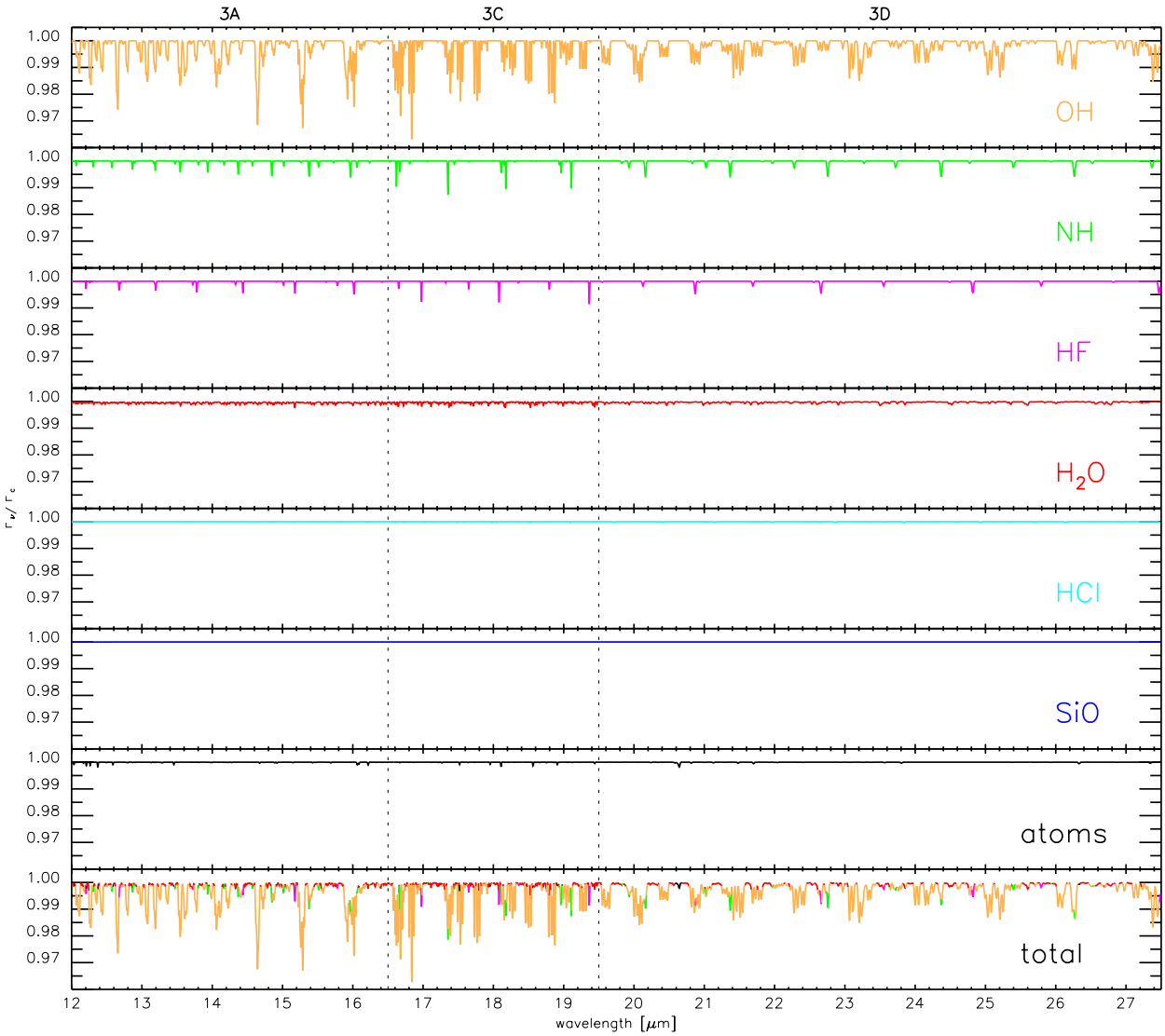

Fig. 7. Relative contribution of the atoms and molecules for α Boo in the wavelength range 12–27.5 μm. The adopted parameters can be found in Table 2. All synthetic spectra are based on the same model atmosphere. The total spectrum coincides with the synthetic spectrum discussed elsewhere in this paper and thus includes all atomic and molecular opacities in its calculation by TurboSpectrum.

4.3.1. Shortcomings attributed to modelling

Continuum opacity The MARCS model atmosphere and the TurboSpectrum code were so far developed and tested to produce theoretical atmospheric models and spectra shortwards of 20 μm, and the extrapolation of some assumptions beyond this wavelength is not valid. Problems exist with the continuum opacity computation, leading to small flux jumps (<0.5%) in the *absolute* synthetic spectrum, from about 23–26 μm onwards. In particular, the method of extrapolation of the collision-induced absorption coefficients of H_2 pairs (calculated for temperatures ranging from 1000–7000 K and up to 12.5 μm, Borysow et al. 1997) to the far-IR should be investigated. The effect of the collision-induced H_2–H_2 absorption should be small for our sample stars. This opacity source is important in the near-IR for stars of low effective temperatures, high gravities, and low metallicities (Borysow et al. 1997).

Line strength A second discrepancy is that almost all molecular lines observed with SWS are predicted by the atmospheric models as too weak by a few percent, see Figs. 10, 11, and especially 12. It occurs for the stars the spectrum of which is dominated by OH (α Boo till γ Dra) as well for those dominated by H_2O (α Tau till β Peg). Similar discrepancies, mostly for low-excitation lines, were found by several authors, e.g. by Decin (2000); Decin et al. (2003c) for the OH 1–0 and 2 – 1 lines, and for the ^{12}CO 2–0 and 3–1 lines in the shorter-wavelength range of SWS (2.38–12 μm), and attributed to a problem with the temperature structure in the outermost layers of the photosphere. Ryde et al. (2002) found that they could only reproduce the OH 0–0 and H_2O lines in the high-resolution ($R \sim 80\,000$) 12.2–12.4 μm and 10.8–11.3 μm spectra of α Boo after lowering the temperature structure of the outermost parts of the photosphere w.r.t. a standard MARCS model atmosphere. An excess water absorption in the near-IR

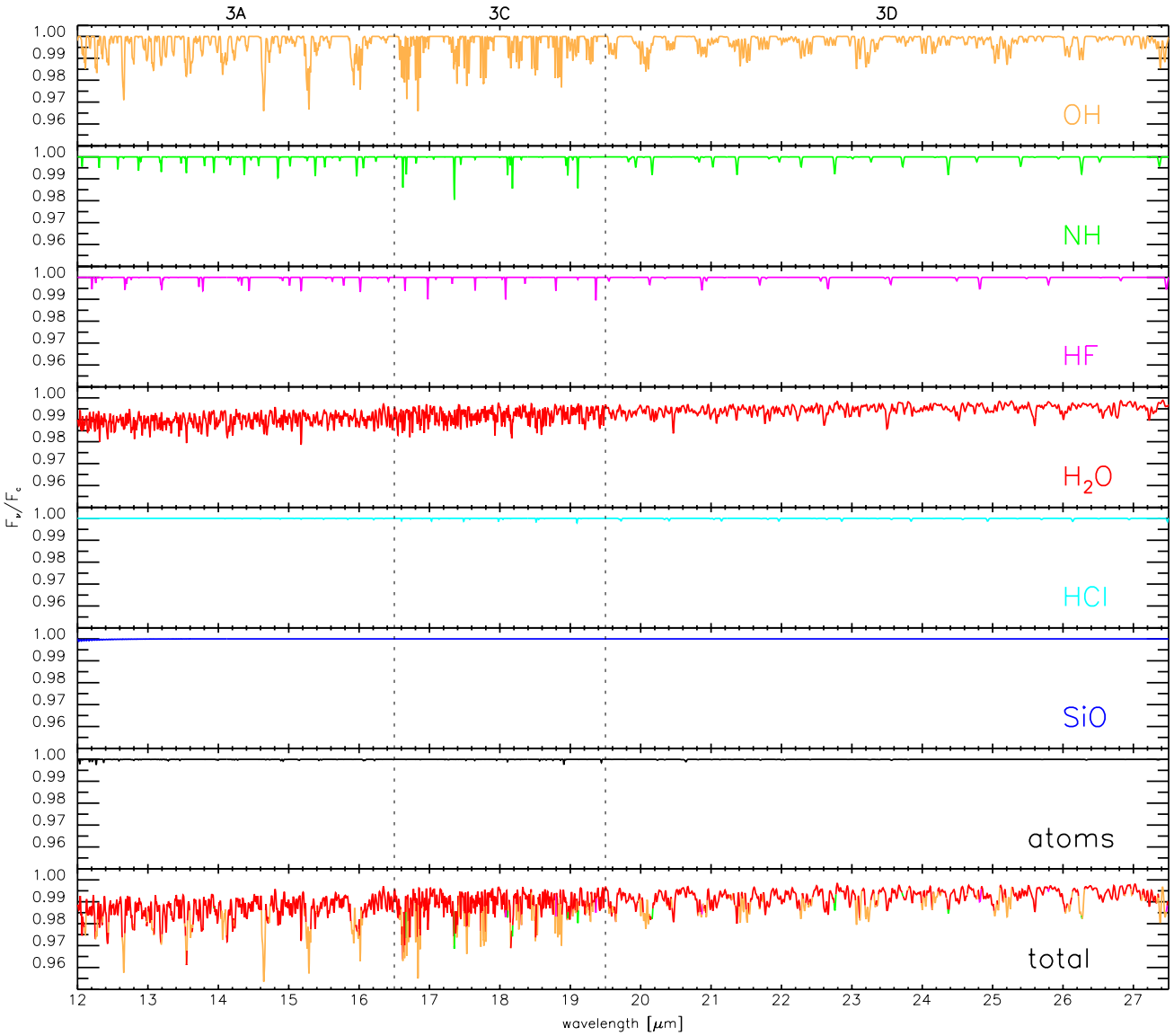

Fig. 8. Relative contribution of the atoms and molecules for α Tau in the wavelength range 12–27.5 μm. The adopted parameters can be found in Table 2. See Fig. 7 for the meaning of the different synthetic spectra.

spectra of late K and M giants and supergiants, had already been reported by Tsuji et al. (1997); Tsuji (2000, 2001); Matsuura et al. (1999, 2002). In order to explain the line depths of the strongest CO fundamental band lines of a number of cool stars, Wiedemann et al. (1994) discarded the chromospheric temperature rise and required the boundary temperature to fall to 2400 K in the highest layers contributing the CO line cores. Ayres (2002) also inferred cool CO gas above the classical temperature minimum in the case of the Sun.

These discrepancies can thus all be attributed to a lower temperature structure in the outer parts of the photosphere than predicted by means of classical model atmospheres. Throughout the IR, the continuous opacity, which is due to H^-_{ff}, is large and grows with wavelength; the continuum is formed quite far out in the atmosphere (ca. τ_{500}[1] = 0.5 at 12 μm) and lines are formed even further out, thus, strong lines are formed in layers where the assumptions of the model atmosphere calculations could not be valid. This temperature stratification problem is thus expected to become larger with IR wavelength. One assumption in particular which should be questioned, is that of a homogeneous atmosphere, as the presence of deep convective envelopes and a chromosphere is well established around some of our sample stars (e.g. α Boo). The chromosphere is dynamic with acoustic waves propagating through the atmosphere, possibly leading to the cooling of the outer atmospheric layers or to the destruction of molecules due to a temperature rise. These latter two effects are variously known as "molecular catastrophe" or "temperature bifurcation" and can also be driven by other mechanisms. Furthermore, the relaxation of the assumption of LTE in the photospheric structure or line formation in the boundary layers of a model atmosphere, could also cause larger strengths for the lines formed in these layers. Possibly, non-chemical-equilibrium calculations might also (partly) account for stronger lines in the mid-IR.

[1] The optical depth calculated at 500 nm.

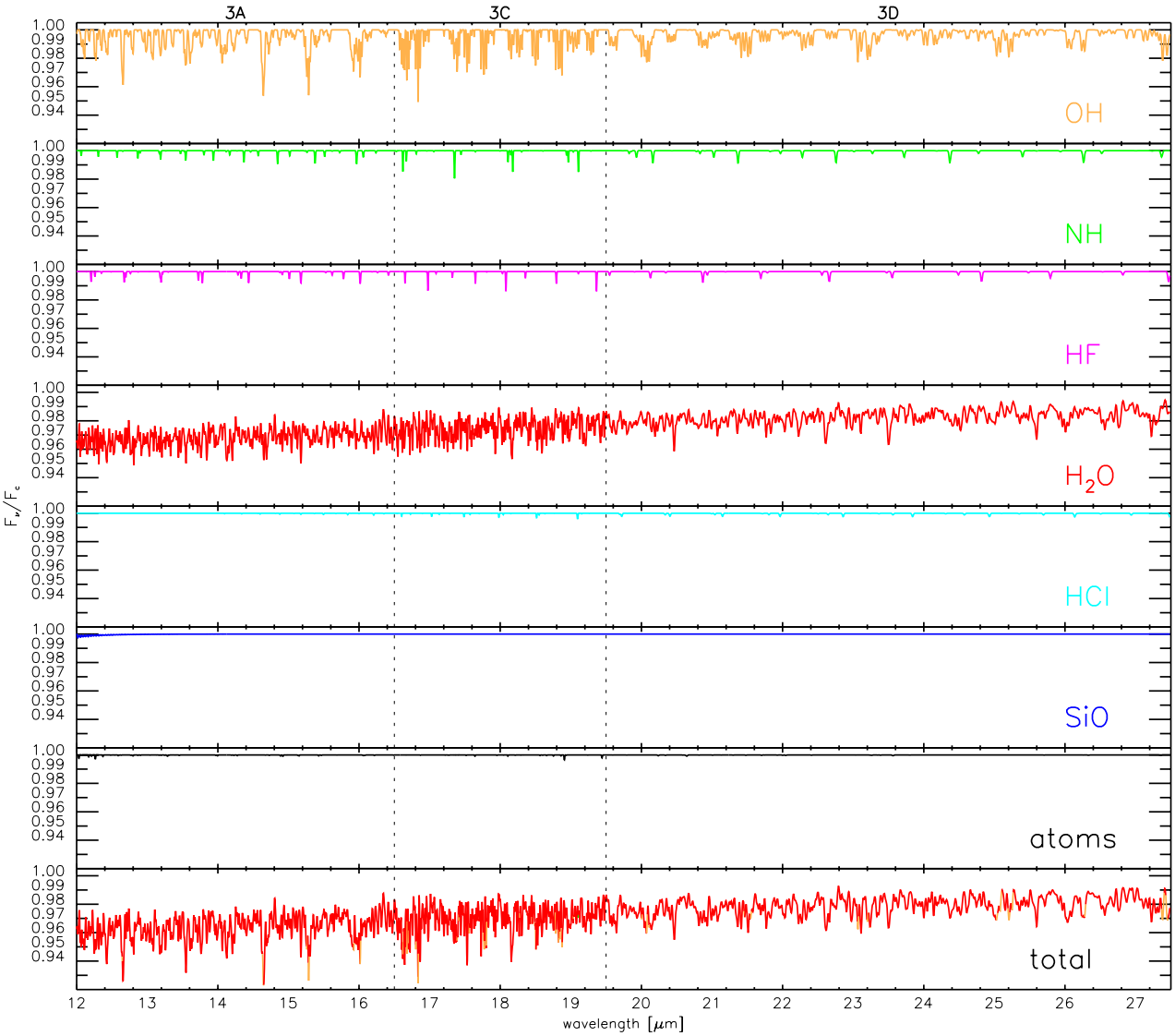

Fig. 9. Relative contribution of the atoms and molecules for β Peg in the wavelength range 12–27.5 μm. The adopted parameters can be found in Table 2. See Fig. 7 for the meaning of the different synthetic spectra.

Total number of lines Another striking difference between the observed and generated spectra for all our sample stars is the total number of lines: the observed SWS spectra contain a large number of lines which have not yet been reported in the relevant literature and hence are not included in our line lists. We refer to Fig. 12, where for band 3A some supposed atomic and molecular lines, (mostly) absent in the synthetic spectra, are indicated with vertical dashed lines. We followed two criteria to call an absorption feature a physical transition line: first, the feature must be detected in both the up- and the downscan, and secondly, the feature must be observed in the stars of our sample having about the same effective temperature. Although we can not fully cancel out features caused by fringing in this way, we believe we are dealing with real physical absorption lines in most of the cases. The figure demonstrates the need for more atomic and molecular line lists for this wavelength region. E.g. the VALD (Vienna Atomic Line Database, Piskunov et al. 1995; Ryabchikova et al. 1999; Kupka et al. 1999), which is a compilation of all atomic data publicly available, did not generate any atomic absorption line at all in our wavelength range for the stellar parameters of the three hottest targets studied!

4.3.2. Instrumental shortcomings

In this section, we give a rather qualitative anthology of the encountered instrumental artifacts in band 3. A quantitative table of these phenomena can be found in the concluding next section.

Fringe residuals After integrating in our reduction process the latest versions of routines developed to remove fringes (version 2.1 of `resp_inter` and version 2.10 of `fringes`, see above), most fringe components are accounted for, but some residual fringes remain. Having *another* look at Fig. 12 (i.e. comparing the different SWS spectra without paying attention to the shown synthetic spectra), some very sharp lines can be detected at the beginning of the band in the spectra of all figured stars. As these lines appear at about the same wavelength

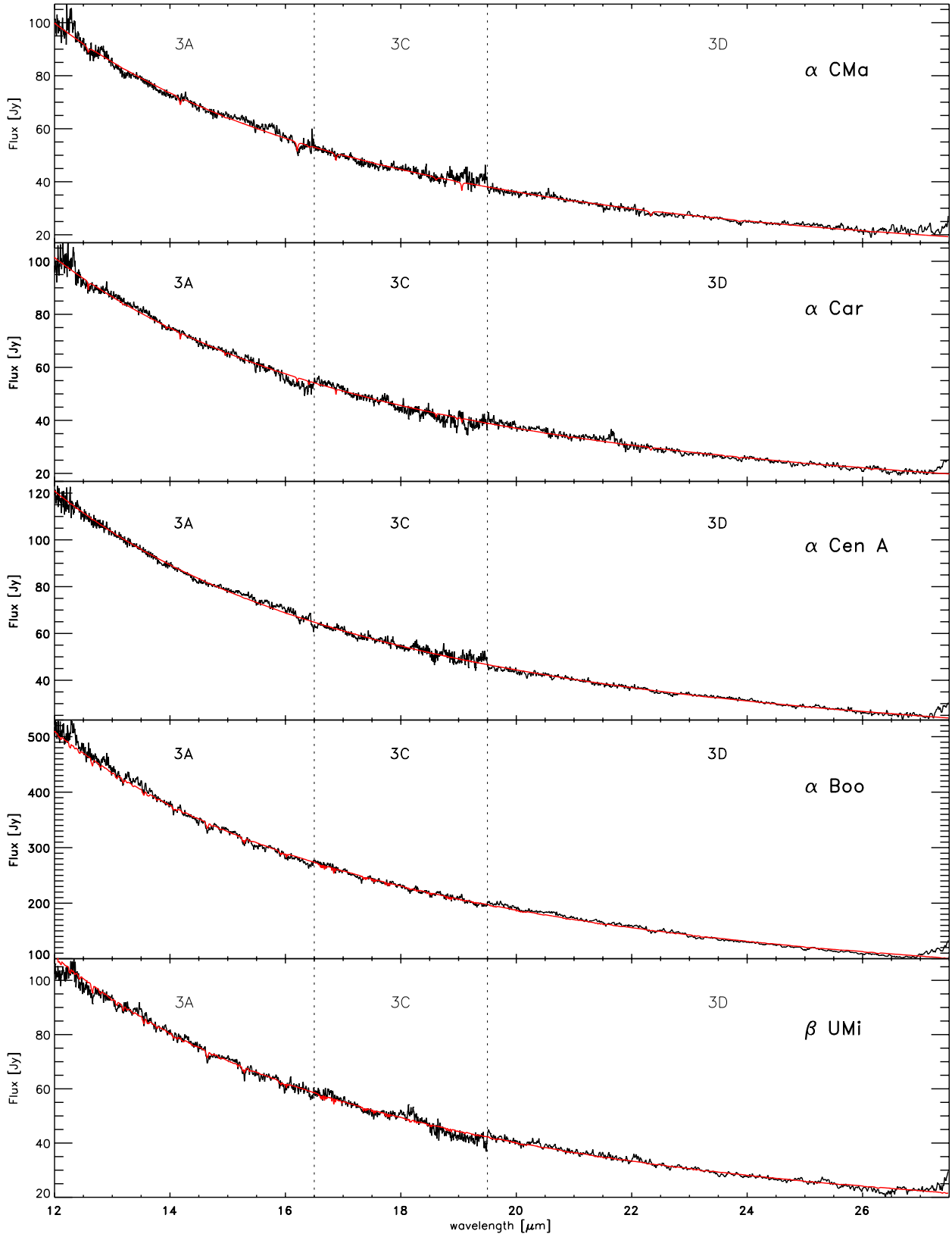

Fig. 10. Global overview of the final modelling (grey) of the SWS bands 3A, 3C and 3D spectra (black) of the 5 hottest stars of our sample.

in the spectra of the hottest as well as of the coolest stars of our sample, their origin must be instrumental, and fringes seem to be the most promising candidates. These fringes are not found by the program `fringes` because they are not present in the entire band, which is a requirement for the model which `fringes` uses. So we have to conclude that this model is incomplete.

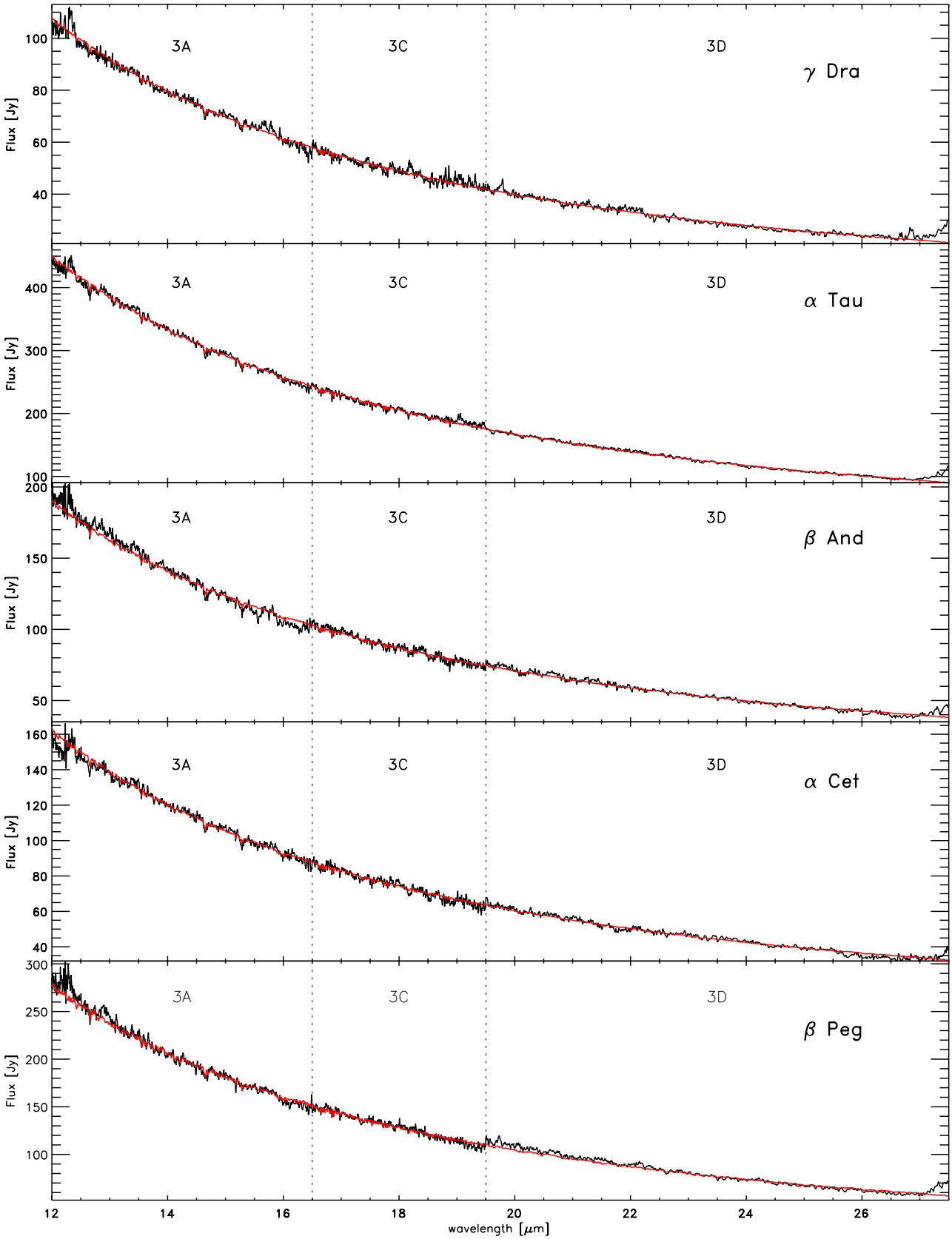

Fig. 11. Global overview of the final modelling (grey) of the SWS bands 3A, 3C and 3D spectra (black) of the 5 coolest stars of our sample.

Another test on the fringe removal by `resp_inter` & `fringes` is provided through the comparison of the reduced spectrum with the RSRF. This is done for β Peg and α Cen A in Fig. 13. For β Peg, we also figured the spectrum reduced without defringing. The fringe pattern of the RSRF is clearly reflected in this spectrum. The fringes occur at exactly the same

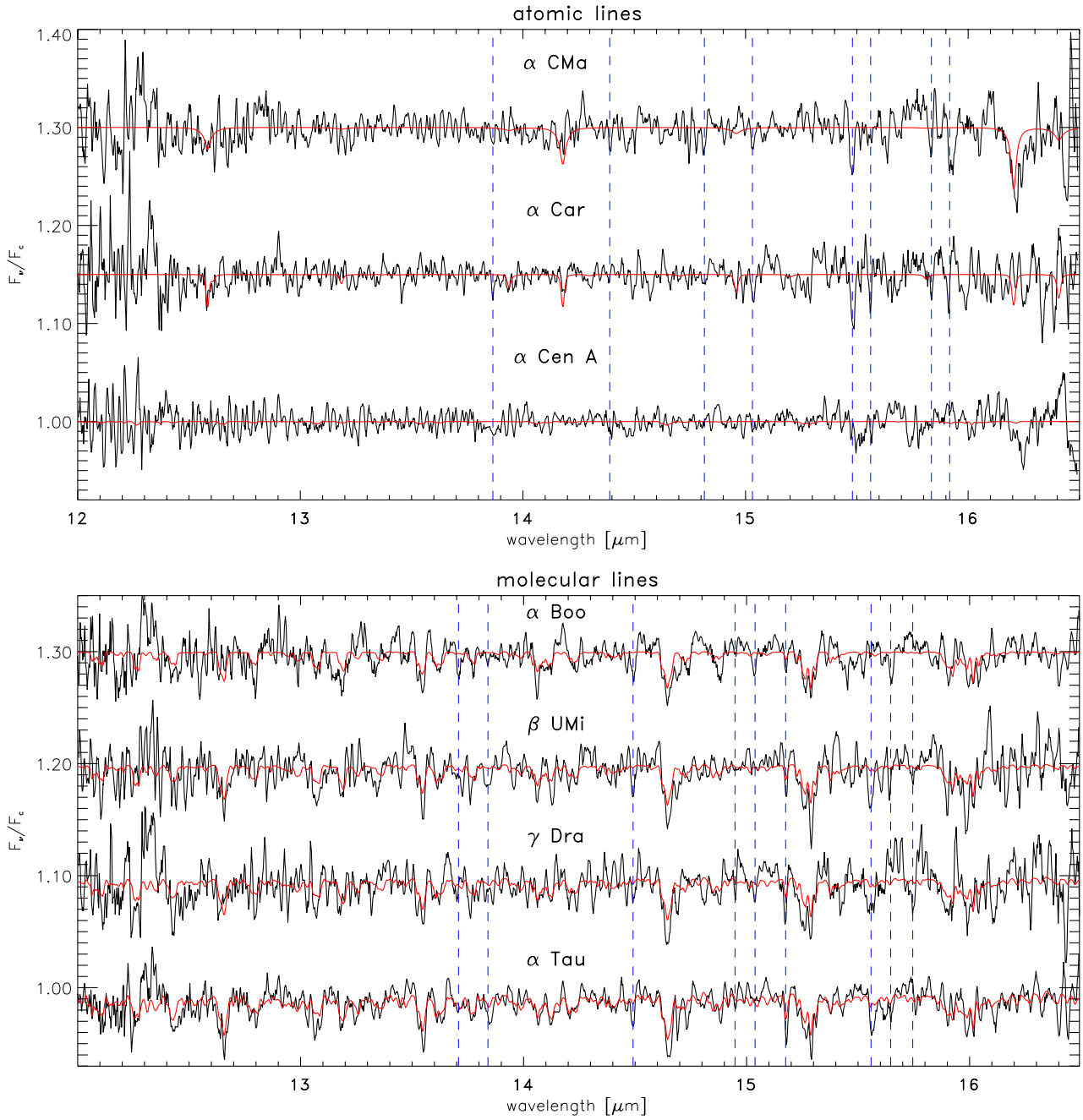

Fig. 12. Suspected atomic (top panel) and molecular (bottom panel) lines in the SWS spectra (black), but absent in the synthetic spectra (grey). The SWS spectra are cleaned up a bit, by dividing out some remaining instrumental response artifacts, see Fig. 14, in order to enable a more detailed comparison with the synthetic spectra. Spectra are offset. The broad feature at 12.3 μm is a residue of an artifact in the RSRF.

wavelengths in both the RSRF and the fringed spectrum and their amplitude can locally amount up to 10% in this wavelength region of the observed spectrum. Unfortunately, some of these fringes survive in our defringed spectrum, marked by vertical dotted lines in Fig. 13. The marked features are indeed fringes, as their wavelengths do not coincide with spectral lines in our (incomplete) synthetic spectrum and as the features do not fulfill the requirements for our definition of a spectral line, used in Sect. 4.3.1. In the SWS spectrum of α Cen A, features can be identified with fringes in the RSRF. However, a large number of very sharp lines in the observed spectrum is completely absent in the RSRF of this band. Noise cannot be responsible, since neighbouring points are correlated; as a matter of fact, the observed correlation is typical of fringes. On the other hand, a physical origin of these lines is highly unlikely, because they are not present in the synthetic spectrum of α Cen A, nor in the ATMOS spectrum of the Sun, α Cen A's twin.

Baseline ripples *Baseline ripples* represent the apparent oscillation of the observed spectra around the synthetic spectra, which is present for all our stars. In order to qualify this

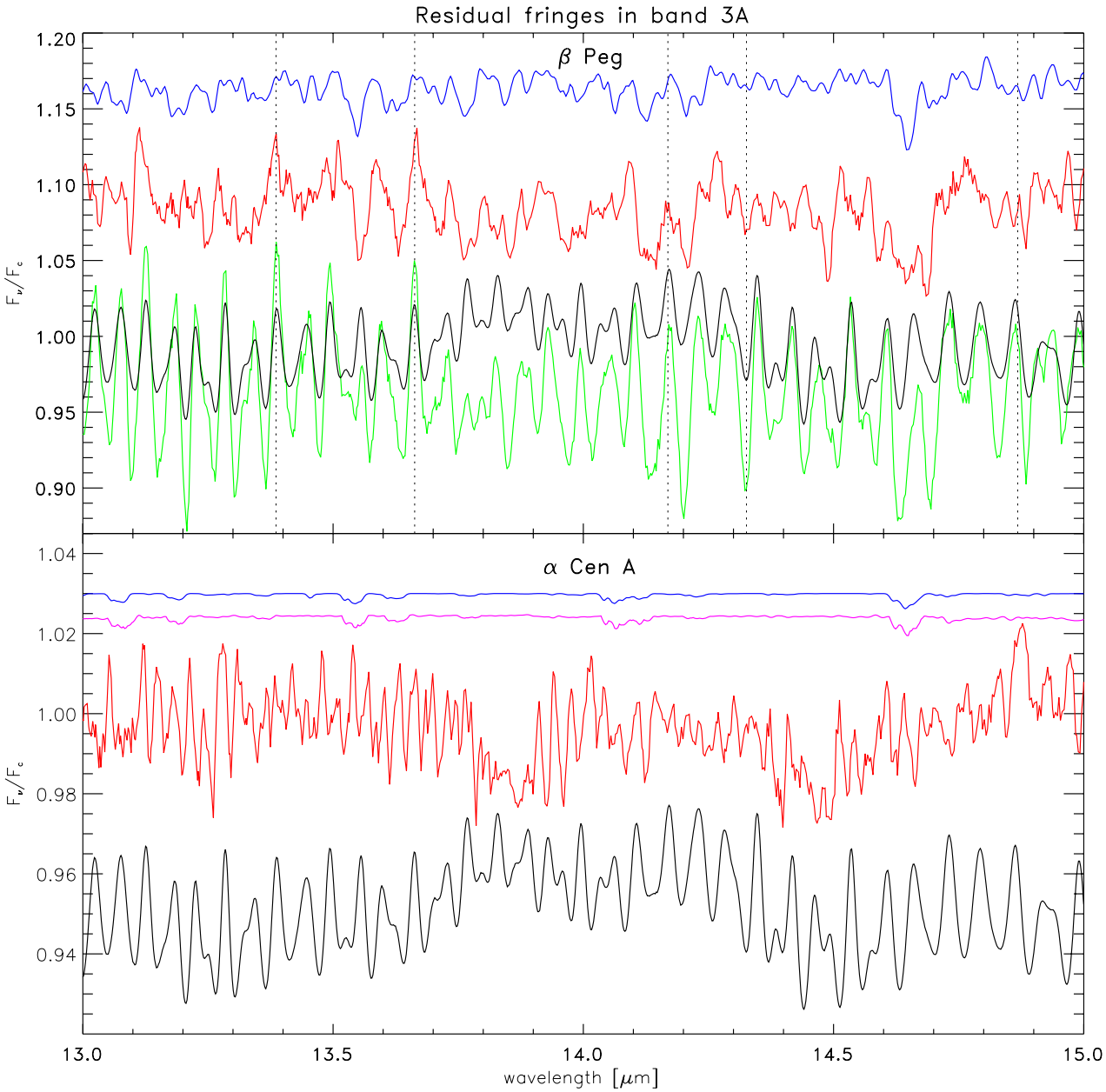

Fig. 13. Two examples of residual fringes in band 3A. The (scaled and shifted) RSRF are displayed in black, the final reduced – defringed – spectra in mid-grey, synthetic spectra in dark grey (uppermost spectra). Spectra are offset and normalised.
Top panel: For β Peg, we also included the spectrum reduced without defringing in light grey (lowest). In this spectrum, the fringe pattern of the RSRF can easily be recognised. Some of these fringes still survive (see the vertical dotted lines) after fringe removal.
Bottom panel: In the spectrum of α Cen A, the fringe pattern of the RSRF is detected. Additionally, the spectrum contains fringes at wavelengths which can not be identified with the fringes of the RSRF. The light grey spectrum is the ATMOS (Atmospheric Trace Molecule Spectroscopy, Farmer et al. 1989; Geller 1992) spectrum of the Sun, α Cen A's twin.

suspected instrumental induced oscillation, we divided our reduced, normalised SWS spectra with the synthetic spectra and rebinned these quotients at low resolution (typically 50). These quotients are for each band and for all stars plotted above each other in Fig. 14. Especially in band 3A, one unique oscillating trend in all stars can be roughly reported (i.e. minima and maxima at more or less the same wavelengths), with the exception of the band edges, where we distinguish a variety of trends. The latter are due to the worse calibration and reduction at these wavelengths: the incomplete removal of fringe components, residual RSRF artifacts at 12.3 μm, etc. When comparing the baseline ripples obtained from spectra of different speeds of one star (see Fig. 15), we reach the same conclusions.

The origin of the baseline ripples is probably related to the fringes. When the signal passes through the fringing FPs, some of the flux is reflected backward; if the signal were divided by a perfect RSRF this lost flux would be restored. In reality, the signal is divided by a not quite adjusted RSRF,

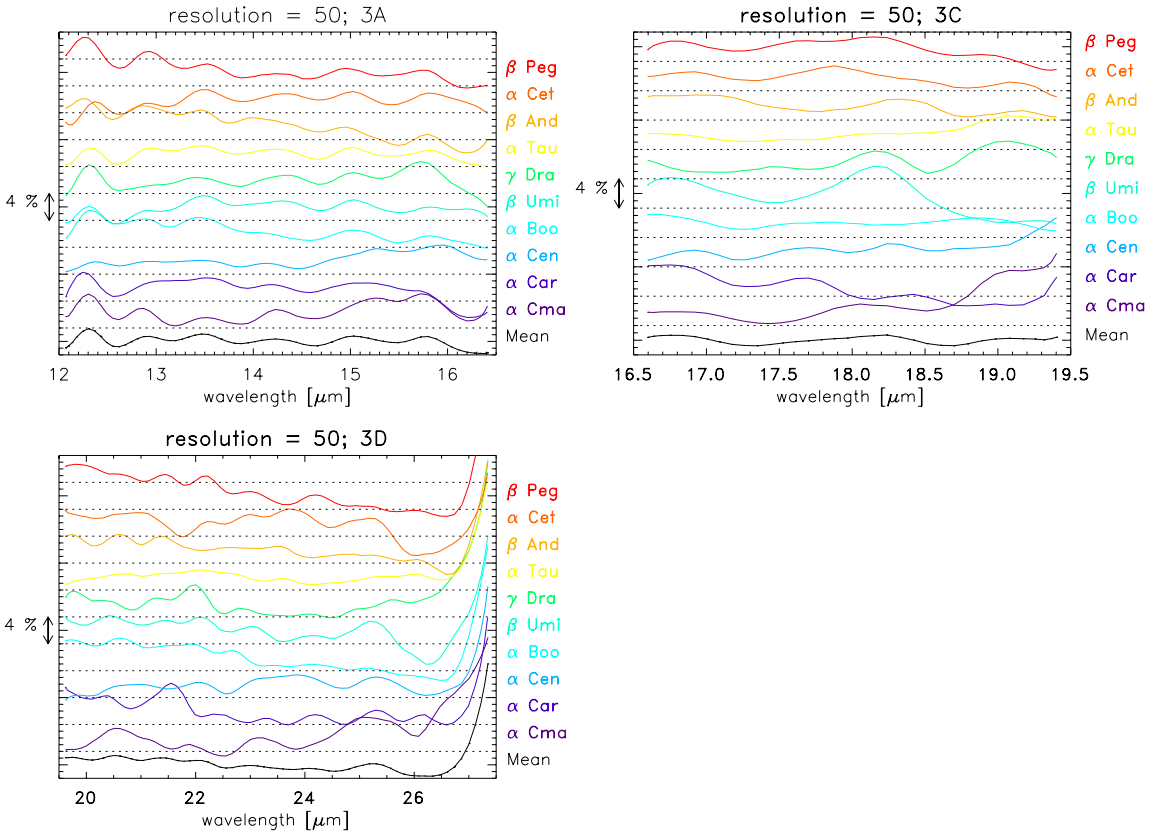

Fig. 14. Division between the SWS spectra and their synthetic spectra at a resolving power of 50, ordered by spectral type. The mean of all these calculated "RSRFs" is shown at the bottom of the figures.

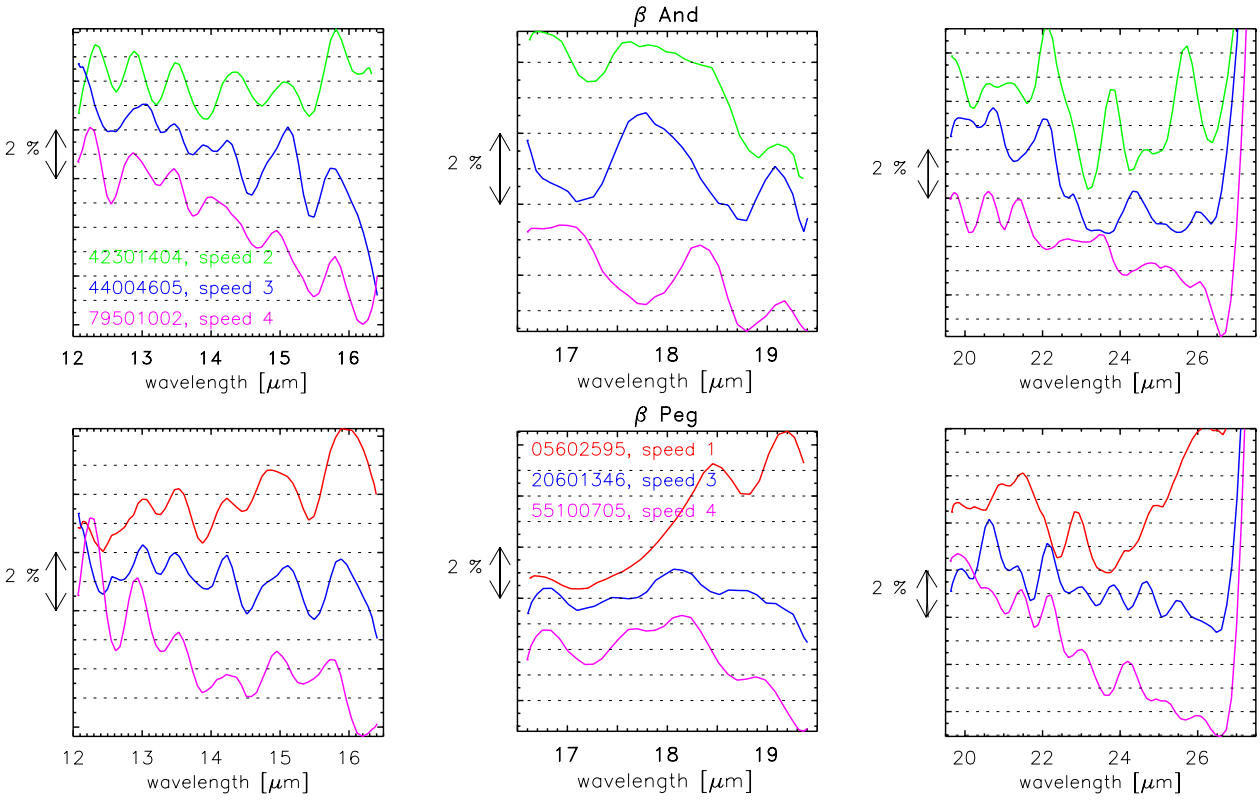

Fig. 15. Division of SWS spectra of different speeds and the synthetic spectra at resolution 50 for β And and β Peg.

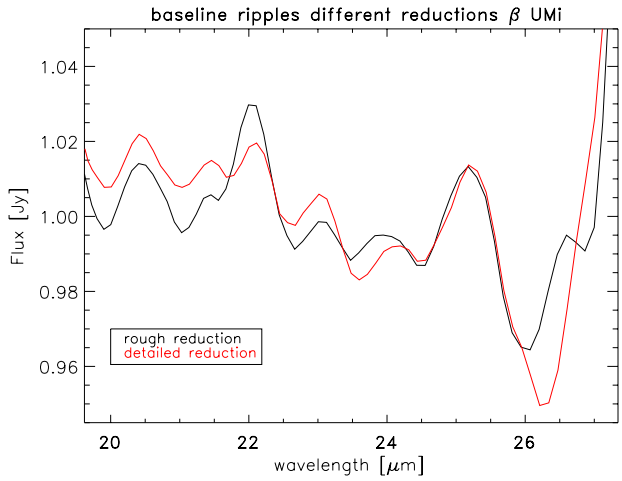

Fig. 16. Example of how the reduction strategy, i.e. with or without glitch and bad detector points removal, affects the phase and amplitude of the baseline ripples present in the SWS band 3 spectra.

even when using `resp_inter`, and any of the following things might happen: when dividing by a RSRF which is too weak, but properly aligned in wavelength, one still misses signal in the original fringes; when the RSRF has too strongly peaked fringes, one actually ends up with too much signal: the fringes invert; and, finally, when the amplitude of the fringes is perfect but the fringes are out of phase, a signal emerges which is right on average but still has shifted fringes. So, in all cases, residual fringes occur, the origin of which is hard to trace. After removal of these residual fringes, the emerging continuum flux might be too small, too large, or just right (Leech et al. 2003). The presence of the baseline ripples in our data points to the occurrence of the first two possibilities. These baseline ripples have an amplitude of a few percent (see Figs. 14 and 15) and they are shaped quite like the envelope of the fringe pattern on the RSRF (see Figure 4 in Kester et al. 2003).

As the wavelength of a baseline ripple is larger than a typical molecular feature in this wavelength range (see Figs. 7–9), it is *not* dangerous to manipulate the baseline ripples. However, every attempt to get rid of these baseline ripples has stranded so far, because of the complexity of the problem. The construction of an adapted RSRF, for example the convolution of the pipeline RSRF with the mean of the rebinned quotients of SWS spectra and synthetic spectra of our standard stars, as shown in Fig. 14, is hampered by the shifts in the peak positions and the differences in amplitudes of the baseline ripples. These phase and amplitude differences may result from pointing errors and reduction strategies, see Fig. 16. Another attempt, namely adding the new optional parameter FILL to `fringes` in order to (partly) add or subtract the envelope of the fringe complex back into the data, was also unsuccessful in removing the baseline ripples from the data. Finally, we stress the fact that no correlation has been found between the amplitude of the baseline ripples and the resolution of the spectrum (see again Fig. 15), although there is a clear relationship between the amplitude of the fringes and the resolution.

Systematics in detector noise Through our reduction process, we carefully compared data for every single detector with the combined data of all detectors. Whenever data from a detector, after flatfielding, deviated too much from the combined data, we eliminated them. Detectors affected by glitches are not taken into account in this discussion. At the reduction of all the spectra of our standard stars, we mostly discarded data from detectors 36, 34, 31, and 29, in this order. Which detectors in a band are reliable and which not, can change. For example, it is known (Leech et al. 2003) that at the start of the mission band 3 detector 34 was poor. After Performance Verification, its bias voltage was changed, and from then on, detectors 30, 31 and 36 were the worst in that band. In general a bad detector has either a high dark current or/and a high noise. The average detector dark noise of band 3 is the highest of all SWS bands, equalling a value of 3.00 μV/s, whereas this quantity is 0.70, 1.50 and 2.00 μV/s for bands 1, 2 and 4 respectively. Checks were made at the start of every revolution to characterise the dark current and noise throughout the mission. It was found that they were stable for all bands except band 3. Here, the dark currents increased by up to a factor of three during the mission. In most cases the increase in dark currents was gradual, but occasionally there was a sudden increase in the trends of dark currents, e.g. detector 36 during revolution 150 (Leech et al. 2003).

Leakage In all our spectra, we notice in band 3D a flux increase from about 26.5 μm onwards compared to the synthetic spectra (see e.g. Figs. 10 and 11). This feature is a known instrumental artifact and is due to leakage from 13–14 μm photons: the order selection filters in the light path of band 3D appear not to cut off the shorter wavelengths sufficiently well. This leakage is maximally about 40% in our observations. It primarily affects objects with flux declining sharply towards long wavelengths, as is the case for all our sources. For sources that have a relatively low flux at 14 μm compared to 28 μm, the RSRF for band 3D is appropriate and hence such sources suffer no leakage. The light leak at the long wavelength end of band 3D in blue sources, rendering observations around 28–29 μm problematic, led to the introduction of band 3E after the Performance Verification phase (Leech et al. 2003). However, the calibration of band 3E is not quite successful, as it is hampered by the low signal-to-noise ratio of most sources in this wavelength region. The same reason prevented us from taking band 4 into account in our study, as (1) no in-orbit correction of its RSRF could be determined due to the lack of suitable (i.e. with a decent S/N) calibration targets with a well known energy distribution in the region 30–45 μm, (2) the dark current subtraction gets problematic for low-flux sources (resulting in unreal negative fluxes in the AAR product), (3) single detector jumps arise at low-signal levels. In particular, band 4 also suffers from memory effects, which could not be modelled so far for the detector material used in band 4 and which introduce errors at the 8–30% level for high fluxes (>100 Jy). These memory effects give the strong and frequent glitches long tails in band 4.

Band-to-band discontinuities Finally, consider Table 1, where the weighted scaling factors of the different bands are shown; these are an indication of the reliability of the absolute and relative flux calibration of the SWS instrument. From this table, no trends or correlations of the strength of the scaling factors with for example revolution number, speed, flux level, etc. can be determined. However, it is remarkable that the largest deviations from unity take place for the stars with the highest flux level (α Boo, α Tau, β Peg and β And) in our range of speed 4 spectra. Several phenomena cause the scaling factors between different bands of an observation and between different observations of a given star: uncertainties in the flux calibration, the low responsivity at the band edges, *pointing errors*, and a *problematic dark current subtraction in combination with the RSRF correction*, from which the pointing errors are believed to have the largest impact. The pointing errors as well as the RSRF correction cause a decrease of the flux level by a gain factor, where the dark current subtraction can lower the flux level by an offset. As the effects of the pointing errors and the RSRF correction are estimated to be larger than the dark current subtraction, we chose to multiply with factors rather than using offset values. We will discuss now the phenomena – written in italic – which are most relevant for band 3.

The spatial response on the sky, or in other words the profile of the beam eventually illuminating the SWS detectors, is determined by the telescope diffraction and the re-imaging of the entrance pupil onto the detectors by the SWS optics (Vandenbussche 2002). The beam profiles are different for every band and are not simple flat-topped functions (see e.g. Figs. 8.1–8.3 in Leech et al. 2003). As a result, if a point source is observed with a pointing offset from the centre of the SWS aperture, the signals in the different bands are reduced by band-dependent factors. Thus, *pointing offsets* can be recognised in the data by jumps in the continuum level at band edges; for example, a star offset from the centre of the aperture by $6''$ in the cross-dispersion direction leads to a loss of approximately 40% in throughput at 17 μm (Leech et al. 2003). During the ISO mission several stars were observed every few weeks for purposes of wavelength and flux calibration. The flux of one of these targets, γ Dra, was seen to show a band 3 modulation of 13% suspected to be due to pointing errors (Feuchtgruber 1998).

The *propagation of RSRF features to the spectra after wrong dark subtraction* depends on the RSRF in the wavelength region affected. The SWS RSRFs show steep slopes at the ends of the bands, and various bands show distinct features in their RSRF. The RSRF correction has to be applied on data for which a proper offset correction is done, i.e. the dark current subtraction has to be done properly. Dividing poorly dark subtracted data by the RSRF will induce false shapes in regions where the RSRF shows features or where the RSRF has a steep slope. Poor matches between different bands can often be understood from (and corrected for) such a combination of dark current uncertainties and a steep RSRF in the overlap region (Leech et al. 2003). A problematic dark current subtraction (for example deduced from a wrong dark current measurement) can also be responsible for a slight shift in the flux level of different observations.

From Fig. 4 and through Tables 1 and 3 a fairly good agreement between the IRAS-PSC fluxes at 12 and 25 μm and the (unshifted) SWS band 3 spectra can roughly be deduced. It does not make sense to try to quantify this relationship due to several major calibration problems we encounter when convolving the SWS spectra with the IRAS 12 and 25 μm survey pass-bands: as these latter extend from 7 to 15.5 μm and from 16 to 31.5 μm respectively, the memory effects in band 2C, the flux leak at the end of band 3D, the unsuccessful calibration in band 3E and of course the relative shifts of the different SWS bands w.r.t. each other have together a large impact on the flux densities at 12 and 25 μm deduced from the SWS spectra. Moreover, the estimated photometric calibration accuracy of bands 2C and 3A is worst around 12 μm and amounts to 14% at this wavelength. The same arguments hold for the confrontation of SWS and LRS data.

5. Conclusions and implications

Modelling the wavelength range 12−27.5 μm of the ISO–SWS draws a light on both the status of the model computation at these wavelengths and of the calibration of bands 3A, 3C and 3D, where some instrumental artifacts have already been mentioned before. Improvements on both aspects require a careful cross-correlation between them. We were able to point at some shortcomings in both domains, although the related solution was often lacking. However, our validation of a consistent set of synthetic spectra in the mid-IR may be of some importance in the broader context of future IR space missions (Herschel, SIRTF, ASTRO-F, etc.) which try to extend the observable IR range to longer wavelengths. We now give a quick overview of the encountered discrepancies, draw conclusions on the reached accuracies with ISO–SWS and formulate some suggestions for future missions from the lessons learnt.

From the modelling point of view, the synthetic spectrum computation is hampered by the lack of comprehensive molecular and atomic line lists for this wavelength range. We also suspect some problems with the temperature distribution in the outer layers of the atmosphere model and inaccuracies in the extrapolation method of the collision-induced absorption coefficients of H_2 pairs to longer wavelengths. Concerning the calibration of bands 3A, 3C, and 3D, we reported the detection of baseline ripples in the observed SWS spectra. We could attribute them to erroneous restauration of spurious Fabry-Pérot effects in the light path. As these baseline ripples can have amplitudes of typically a few percent (see Table 5), they could be mistaken as broad molecular or dust absorptions/emissions in some classes of stars. In future missions special attention should be paid during the design to *suppress* spurious Fabry-Pérot effects.

The sensitivity requirements in a spectral band determine the choice of the detector material, which induces different artifacts in the data which severely limit the accuracy of the calibration. In the case of SWS, the Si:Ga detectors of band 2 induce memory effects, which introduce calibration errors of the order 6−15%, the Si:As detectors of band 3 give rise to fringes with amplitudes in the RSRF up to 25% for band 3A and 17% for bands 3C and 3D, and the Ge:Be detectors of

Table 5. Estimated uncertainties of the different instrumental artifacts present in band 3 for the 10 AOT 01 speed 4 spectra of our sample of standard stars.

Uncertainty source	**3A**	**3C**	**3D**
bad detector data points, scan jumps & glitches	~2%	~2.5%	~4%
fringe residuals			
before correction with `resp_inter` & `fringes`	~8%	~4%	~3%
after correction with `resp_inter` & `fringes`	~2%	~2%	~2%
baseline ripples	~2%	~2%	~1%
leakage at 27.5 μm [a]			~30%
RSRF artifact at 12.3 μm	~4%		
Photometric calibration (scaling factors) [b]	~6.5% (~9.5%)	~5.5% (~9.5%)	~9% (~12%)

Notes:

[a] Calculated as $F_{27.5\,\mu\mathrm{m}}/G_{27.5\,\mu\mathrm{m}}$ with F the flux of the SWS spectrum, G the flux of the synthetic spectrum.

[b] The estimated errors originate from our scaling factors. Between brackets: the mean of the scaling factors, with inclusion of higher scanner speed observations of the sample of standard stars.

band 4 also cause memory effects, with even larger calibration errors (8−30%) (Leech et al. 2003). In this paper, we showed that the Off-Line Processing is unable to completely cancel out these artifacts in the case of the fringing, even when using supplementary reduction tools: fringe residuals of the order of 2% can still be present in the final spectra (see Table 5). It thus remains important that one reduces the data in a self-consistent way oneself, using the provided supplementary tools, rather than relying on the automatic processing; the pipeline processing is in many cases too general for the reduction of the data of a specific target. For high-flux sources, the use of `fringes` should be considered; for low-flux sources, glitches more commonly affect the spectra. In all cases, band-to-band discontinuities have to be corrected for. Two examples for data improvement such supplementary tools can yield, can be derived from Table 5: using the combination `resp_inter` & `fringes` and the (soon publicly available) tool for removal of bad detector data points, scan jumps and glitches led respectively to ~1−6% and ~2−4% improvements in the case of our dataset.

The synthetic spectra of our standard stars offer us the opportunity to determine the scaling factors of the different subbands of band 3, in order to construct a continuous spectrum. These gain factors for the different subbands, as well as between different measurements of a source, are mainly a consequence of pointing errors and the combination of a problematic dark current subtraction with the RSRF correction. The determined scaling factors are indicative for the absolute and relative flux calibration of band 3 and lie generally well between the error bars proposed in Leech et al. (2003) for the photometric calibration accuracy after Off-Line Processing: 12% for band 3A, 10% for band 3C, and 13% in the case of 3D (see again Table 5). The inaccuracies introduced by the RSRF correction depend on the availability of high signal-to-noise ratio measurements of calibration targets with a known energy distribution. The latter may be problematic in the long-wavelength range; the extension of the calibrators with Solar System objects, which have high flux densities in this wavelength range, did not contribute to a better calibration of ISO–SWS, due to errors caused by ISO tracking problems of the fast moving Pallas and Ceres, which were initially proposed. For band 3, the stellar composites of Cohen et al. (1992) were used for the photometric calibration. It is extremely important to build up a large set of calibration targets (including the brightest stars of our sample, α Boo, α Tau, β Peg and β And and the planet Uranus) and to set up a detailed calibration strategy in advance for future IR satellites. Even then, the number of surprises in the calibration process will be high, as we learnt from the pioneering ISO mission.

Acknowledgements. The research has been financed by the Research Council of the KULeuven, grant OT/00/13. We are very grateful to the anonymous referee, whose critical remarks improved the paper substantially. We are also indebted to the editor for helpful comments on the style.

References

Anders, E., & Grevesse, N. 1989, Geochim. Cosmochim. Acta, 53, 197
Aringer, B., Kerschbaum, F., & Jörgensen, U. G. 2002, A&A, 395, 915
Arunan, E., Setser, D. W., & Ogilvie, J. F. 1992, J. Chem. Phys., 97, 1734
Assendorp, R., Bontekoe, T. R., de Jonge, A. R. W., et al. 1995, A&AS, 110, 395
Aumann, H. H., Beichman, C. A., Gillett, F. C., et al. 1984, ApJ, 278, L23
Ayres, T. R. 2002, ApJ, 575, 1104
Borysow, A., Jorgensen, U. G., & Zheng, C. 1997, A&A, 324, 185
Cami, J. 2002, Ph.D. Thesis, University of Amsterdam
Cohen, M., Walker, R. G., Barlow, M. J., & Deacon, J. R. 1992, AJ, 104, 1650
Cohen, M., Witteborn, F. C., Bregman, J. D., et al. 1996, AJ, 112, 241
de Graauw, T., Haser, L. N., Beintema, D. A., et al. 1996, A&A, 315, L49
Decin, L. 2000, Ph.D. Thesis, Catholique University of Leuven, Department of Physics and Astronomy
Decin, L., Waelkens, C., Eriksson, K., et al. 2000, A&A, 364, 137

Decin, L., Vandenbussche, B., Waelkens, C., et al. 2003a, A&A, 400, 709
Decin, L., Vandenbussche, B., Waelkens, C., et al. 2003b, A&A, 400, 695
Decin, L., Vandenbussche, B., Waelkens, C., et al. 2003c, A&A, 400, 679
Edlén, B. 1966, Metrologia, 2, 71
Farmer, C. B., Norton, R. H., & Geller, M. 1989, A high-resolution atlas of the infrared spectrum of the Sun and Earth atmosphere from space: A compilation of ATMOS spectra of the region from 650 T O 4800 cm-1 (2.3 to 16 μm) (Washington, D.C.: National Aeronautics and Space Administration, Scientific and Technical Information Service, 1989–1992)
Feuchtgruber, H. 1998, Status of study on Gam-Dra fluxes and related pointing errors (ISO–SWS online documentation)
Geller, M. 1992, A High-Resolution Atlas of the Infrared Spectrum of the Sun and Earth Atmosphere from Space. Volume III. Key to Identification of Solar Features (Washington, D.C.: NASA, Scientific and Technical Information Division)
Geller, M., Farmer, C. B., Norton, R. H., Sauval, A. J., & Grevesse, N. 1991, A&A, 249, 550
Goldman, A., Brown, L. R., Schoenfeld, W. G., et al. 1998a, J. Quant. Spectrosc. Radiat. Transfer, 60, 825
Goldman, A., Schoenfeld, W. G., Goorvitch, D., et al. 1998b, J. Quant. Spectrosc. Radiat. Transfer, 59, 453
Goorvitch, D. 1994, ApJS, 95, 535
Grevesse, N., Lambert, D. L., Sauval, A. J., et al. 1990, A&A, 232, 225
Gustafsson, B., Bell, R. A., Eriksson, K., & Nordlund, Å. 1975, A&A, 42, 407
Henyey, L., Vardya, M. S., & Bodenheimer, P. 1965, ApJ, 142, 841
Hirata, R., & Horaguchi, T. 1995, Atomic spectral line list, `http://cdsweb.u-strasbg.fr/htbin/Cat?VI/69`
Jones, H. R. A., Pavlenko, Y., Viti, S., & Tennyson, J. 2002, MNRAS, 330, 675
Jørgensen, U. G., Jensen, P., Sørensen, G. O., & Aringer, B. 2001, A&A, 372, 249
Jørgensen, U. G., Larsson, M., Iwamae, A., & Yu, B. 1996, A&A, 315, 204
Kester, D. J. M. 2003, in The calibration legacy of the ISO Mission, proceedings of a conference held Feb. 5–9. 2001, ed. L. Metcalfe, A. Salama, S. B. Peschke, & M. F. Kessler, published as ESA Publications Series, ESA SP-481, European Space Agency, 2003, 243
Kester, D. J. M., Beintema, D. A., & Lutz, D. 2003, in The calibration legacy of the ISO Mission, proceedings of a conference held Feb. 5–9. 2001, ed. L. Metcalfe, A. Salama, S. B. Peschke, & M. F. Kessler. Published as ESA Publications Series, ESA SP-481. European Space Agency, 2003, 375,
Kupka, F., Piskunov, N., Ryabchikova, T. A., Stempels, H. C., & Weiss, W. W. 1999, A&AS, 138, 119
Kurucz, R. L., & Bell, B. 1995, Atomic Line Data (Kurucz CD-ROM No. 23. Cambridge, Mass.: Smithsonian Astrophysical Observatory)
Langhoff, S. R., Bauschlicher, C. W., & Taylor, P. R. 1989, J. Chem. Phys., 91, 5953
Langhoff, S. R., & Bauschlicher, C. W. J. 1993, Chem. Phys. Lett., 211, 305
Le Roy, R. J. 1999, J. Mol. Spectrosc., 194, 189
Leech, K., Kester, D., Shipman, R., et al. 2003, The ISO Handbook, vol. V - SWS – The Short Wavelength Spectrometer
Lorente, R. 1998, Spectral Resolution of SWS AOT 1 (ISO–SWS online documentation)
Matsuura, M., Yamamura, I., Cami, J., Onaka, T., & Murakami, H. 2002, A&A, 383, 972
Matsuura, M., Yamamura, I., Murakami, H., Freund, M. M., & Tanaka, M. 1999, A&A, 348, 579
Miller, S., Tennyson, J., Jones, H. R. A., & Longmore, A. J. 1994, in Molecular Opacities in the Stellar Environment, ed. P. Thejll, & U. G. Jorgensen, Proc. IAU Coll. 146, 296
Ogilvie, J. F., Rodwell, W. R., & Tipping, R. H. 1980, J. Chem. Phys., 73, 5221
Partridge, H., & Schwenke, D. W. 1997, J. Chem. Phys., 106, 4618
Piskunov, N. E., Kupka, F., Ryabchikova, T. A., Weiss, W. W., & Jeffery, C. S. 1995, A&AS, 112, 525
Plez, B., Brett, J. M., & Nordlund, Å. 1992, A&A, 256, 551
Plez, B., Smith, V. V., & Lambert, D. L. 1993, ApJ, 418, 812
Rothman, L. S., Camy-Peyret, C., Flaud, J.-M., et al. 2003, J. Quant. Spectrosc. Radiat. Transfer, in preparation
Rothman, L. S., Rinsland, C. P., Goldman, A., et al. 1996, J. Quant. Spectrosc. Radiat. Transfer, 60, 665
Ryabchikova, T. A., Piskunov, N. E., Stemples, H. C., Kupka, F., & Weiss, W. W. 1999, Phys. Scr. T 83, 162
Ryde, N., & Eriksson, K. 2002, A&A, 386, 874
Ryde, N., Lambert, D. L., Richter, M. J., & Lacy, J. H. 2002, ApJ, 580, 447
Schwenke, D. W. 1998, Faraday Disc., 109, 321
Schwenke, D. W., & Partridge, H. 2000, J. Chem. Phys., 113, 6592
Sneden, C., Johnson, H. R., & Krupp, B. M. 1976, ApJ, 204, 281
Tsuji, T. 2000, ApJ, 538, 801
Tsuji, T. 2001, A&A, 376, L1
Tsuji, T., Ohnaka, K., Aoki, W., & Yamamura, I. 1997, A&A, 320, L1
van Hoof, P. A. M. 1998, in Stellar Evolution, Stellar Explosions and Galactic Chemical Evolution, ed. A. Mezzacappa (Institute of Physics Publishing), 67
Van Malderen, R., Kester, D. J. M., Decin, L., Vandenbussche, B., & Waelkens, C. 1999, in Abstracts of the 2nd Austrian ISO Workshop. Atmospheres of M, S and C Giants, ed. J. Hron, & S. Höfner, 79
Vandenbussche, B. 2002, Ph.D. Thesis, Catholique University of Leuven, Department of Physics and Astronomy
Vidler, M., & Tennyson, J. 2000, J. Chem. Phys., 113, 9766
Wallace, L., Bernath, P., Livingston, W., et al. 1995, Science, 268, 1155
Wiedemann, G., Ayres, T. R., Jennings, D. E., & Saar, S. H. 1994, ApJ, 423, 806